Appl. Magn. Reson. 31, 59–98 (2007)

Applied Magnetic Resonance

High-Field EPR, ENDOR and ELDOR on Bacterial Photosynthetic Reaction Centers

A. Schnegg[1], A. A. Dubinskii[2], M. R. Fuchs[1,a], Yu. A. Grishin[3], E. P. Kirilina[1,b], W. Lubitz[4], M. Plato[1], A. Savitsky[1], and K. Möbius[1]

[1] Department of Physics, Free University Berlin, Berlin, Germany
[2] Institute of Chemical Physics, Russian Academy of Sciences, Moscow, Russian Federation
[3] Institute of Chemical Kinetics and Combustion, Russian Academy of Sciences, Novosibirsk, Russian Federation
[4] Max Planck Institute for Bioinorganic Chemistry, Mülheim an der Ruhr, Germany

Received September 29, 2006; revised October 4, 2006

Abstract. We report on recent 95 and 360 GHz high-field electron paramagnetic resonance (EPR), electron–nuclear double resonance (ENDOR) and pulsed electron–electron double resonance (PELDOR) studies of wild-type and mutant reaction centers (RCs) from the photosynthetic bacterium *Rhodobacter sphaeroides*. Taking advantage of the excellent spectral and temporal resolution of EPR at 95 and 360 GHz, the electron-transfer (ET) cofactors radical ions and spin-correlated radical pairs were characterized by their *g*- and hyperfine-tensor components, their anisotropic T_2 relaxation as well as by the dipolar interaction between $P_{865}^{\bullet+}Q_A^{\bullet-}$ radical pairs. The goal of these studies is to better understand the dominant factors determining the specificity and directionality of transmembrane ET processes in photosynthetic RC proteins. In particular, our multifrequency experiments elucidate the subtle cofactor–protein interactions, which are essential for fine-tuning the ET characteristics, e.g., the unidirectionality of the light-induced ET pathways along the A branch of the RC protein. By our high-field techniques, frozen-solution RCs of novel site-specific single and double mutants of *R. sphaeroides* were studied to modulate the ET characteristics, e.g., even to the extent that dominant B branch ET prevails. The presented multifrequency EPR work culminates in first 360 GHz ENDOR results from organic nitroxide radicals as well as in first 95 GHz high-field PELDOR results from orientationally selected spin-polarized radical pairs $P_{865}^{\bullet+}Q_A^{\bullet-}$, which allow to determine the full geometrical structure of the pairs even in frozen-solution RCs.

1 Introduction

Life on Earth is brought about by photosynthesis, the synonym for light-driven energy-, electron- and proton-transfer processes that convert the energy of sun-

[a] Present address: Bessy GmbH, Berlin, Germany
[b] Present address: PTB, Berlin, Germany

light into electrochemical energy needed by higher organisms for cell growth and replication [1, 2]. The "primary processes" of photosynthesis are those in which the incoming light quanta, after being harvested by antenna pigment-protein complexes and channeled to the transmembrane reaction center (RC) protein complexes by ultrafast energy transfer, initiate electron-transfer (ET) reactions between protein-bound donor and acceptor pigments across the cytoplasmic membrane [3]. The successive charge-separating ET steps between the various transient redox partners in the RC have very different reaction rates, k_{ET}. The lifetimes, $t_{1/2} = (k_{ET})^{-1}$, of the intermediary charge-separated states range from less than 1 ps for neighboring donor-acceptor pigments to more than 1 ms for large donor-acceptor separations on opposite sides of the thylakoid membrane. The cascade of charge-separating ET steps of primary photosynthesis competes extremely favorable with wasteful charge-recombination ET steps thereby allowing for almost 100% quantum yield. The largest impact of photosynthesis on life on Earth have green plants and specialized algae. In their photosystems I and II, two RCs that are interconnected by electron transport chains, a reversible catalytic ET photocycle occurs for which water serves as electron donor. Carbon dioxide is fixed in the form of carbohydrates, and oxygen gas is released as a by-product, thereby stabilizing the oxygen content of the Earth's atmosphere.

Three billion years before green plants evolved, photosynthetic energy conversion could be achieved by certain bacteria, for instance, the purple bacterium *Rhodobacter sphaeroides*. These unicellular organisms contain only one RC for light-induced charge separation. They cannot split water but rather use hydrogen sulfide or organic compounds as electron donors to ultimately reduce CO_2 to carbohydrates with the help of sunlight. In Fig. 1 the structural arrangement of the RC of *R. sphaeroides* is shown according to the 0.22 nm resolution X-ray structure by Stowell et al. [4]. The cofactors are embedded in the L, M, H protein domains forming two ET branches, A and B. The RC of the carotinoidless strain R-26.1 of *R. sphaeroides* contains eight cofactors: the primary donor P_{865} "special pair" (a bacteriochlorophyll *a* [BChl] dimer), two accessory BChls (B_A, B_B), two bacteriopheophytins *a* (BPh_A, BPh_B), two ubiquinones (Q_A, Q_B), and one nonheme iron (Fe^{2+}).

As a dominant motif of photosynthetic bacteria, an approximate C_2 symmetry prevails of the cofactor arrangement in the RC. It is intriguing that, despite this pseudo twofold local symmetry of the cofactor arrangement, the primary ET pathway in RCs of purple bacteria is practically one-sided along the A branch ("ET unidirectionality" [5, 6]), as is indicated by the arrows in Fig. 1. It is noted, however, that very recently it was demonstrated that in RCs from wild-type *R. sphaeroides* still a small fraction of native RCs exhibits light-induced reduction of Q_B via the B branch ET [7]. The origin of the unidirectionality enigma of bacterial ET is not yet fully understood at the molecular level, despite the numerous elaborate studies, both experimental and theoretical, performed over the last decades [3, 8, 9]. As a matter of fact, the high-resolution X-ray structure of RCs reveals that the pseudo C_2 symmetry of the cofactors does not pertain to their microenvironment but is broken by different amino acids at symmetry-re-

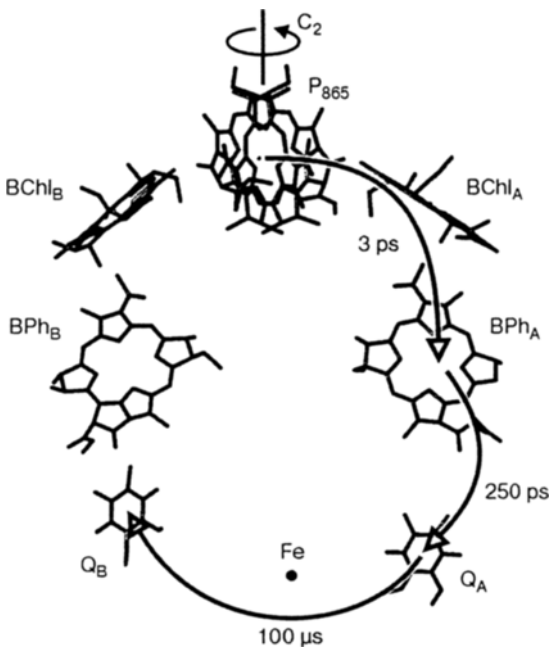

Fig 1. X-ray structure of the cofactor arrangement in the RC from *R. sphaeroides* [4] (PDB entry 1AIJ). The cofactors P_{865} (bacteriochlorophyll *a* dimer), $BChl_A$ and $BChl_B$ (bacteriochlorophyll *a*), BPh_A and BPh_B (bacteriopheophytin *a*), Q_A and Q_B (ubiquinone-10), Fe (Fe^{2+} ion) are related by approximate C_2 symmetry of the protein branches A and B of the RC to which the cofactors bind. The arrows indicate the ET steps with their time constants. Despite the approximate C_2 symmetry of the cofactor arrangement in wild-type RCs, the light-induced ET proceeds almost exclusively along the A branch ("unidirectionality"). For details, see text.

lated sites along the two ET branches. Thereby, the relative redox energetics of the cofactors along the two branches are modulated for establishing conformational gating in favor of the A side and tuned for optimum efficiency of the intermediate states of the cofactors in the ET cascade.

From many genetic engineering experiments it turned out that the ET unidirectionality along the A branch is very robust against point mutations of the amino acid environment of the cofactors in the RC [10, 11]. It was only recently demonstrated that specific double-site mutations in the vicinity of the primary donor and an accessory BChl in RCs from *R. sphaeroides* can drastically change the partition of ET pathways between the A and B branches [9, 12]. Under conditions of high pH and blue-light excitation, up to 100% B branch ET could be achieved [9, 12]. Similar strategies for altering the A and B branch ET partition by strategic point mutations were reported recently by the Feher group [7]. They constructed RCs from *R. sphaeroides* with selected double, triple, quadruple and quintuple mutations. The mutations were introduced sequentially into site-specific positions along the ET pathways. As a result of these mutations, in 95% of the

RCs the ET occurs along the A branch, while 5% of the ET is shifted to the B branch [13]. Apparently, the breakage of symmetry in the ET pathways is largely due to the tuned energetics and electronic couplings of the primary donor and the intermediary acceptors in the RC.

According to the Marcus ET theory [3, 14], the controlling factors of the nonadiabatic ET rate, $k_{ET}(na)$, are the energetics of the redox couple that are contained in the vibrationally averaged Franck–Condon factor F and the electronic coupling matrix element V^2 between donor and acceptor wave functions: $k_{ET}(na) = (2\pi/\hbar)V^2F$. The Franck–Condon factor F is governed by the free energy change ΔE of the reactants and the reorganization energy λ of the final charge-separated state in the equilibrium solvent (i.e., the protein matrix) configuration of the initial state: $F = \exp(-E_a/kT)/\sqrt{4\pi\lambda kT}$ with the activation energy $E_a = (\Delta E + \lambda)^2/4\lambda$. The electronic coupling V^2 is determined by the degree of orbital overlap between the donor and acceptor cofactors. A number of theoretical and experimental studies have embarked on the demanding task to determine the factors F and V^2 for the ET pathways in native and mutant RCs from *R. sphaeroides* (see, for example, refs. 6 and 15–17). Unfortunately, site-selective mutations often affect both F and V^2 simultaneously. By appropriate mutation strategies, however, it is sometimes possible to predominantly modulate either F or V^2 (see below).

For "fast" protein relaxation dynamics, i.e., when the nuclear motion is fast on the ET time scale, nonadiabatic ET prevails with the rate $k_{ET}(na)$. This is the typical situation at room temperature. The critical quantity describing whether the matrix relaxation (approximated by one relaxation time τ_L) is fast or slow on the ET time scale, is the adiabaticity factor κ in the Marcus theory: $\kappa = 4\pi V^2\tau_L/h\lambda$. Two limiting cases are generally considered, the nonadiabatic case with $\kappa \ll 1$, and the adiabatic case with $\kappa > 1$. In the adiabatic case, the solvent dynamics cannot be neglected, and the ET rate becomes solvent-controlled, i.e., $k_{ET}(a)$ is governed by the solvent's longitudinal dielectric relaxation time τ_L. Consequently, the nonadiabatic ET rate in photosynthetic RCs at ambient temperatures has to be corrected in order to describe the adiabatic case: $k_E(a) = k_{ET}(na)/(1 + \kappa)$. The temperature-dependence of τ_L (and thereby of κ) is determined by the temperature-dependent Debye relaxation time τ_D since $\tau_L = (\varepsilon_\infty/\varepsilon_s)\tau_D$. Here, ε_s and ε_∞ are the static and high-frequency (optical) dielectric constants of the solvent medium, respectively.

Thus, an experimental handle to control the transition from the nonadiabatic to the solvent-controlled adiabatic limit is provided by the temperature and by the polarity and the H-bonding capability of the protein microenvironment, i.e., the solvent matrix [3, 18]. Moreover, in addition to the static properties of the protein matrix, dynamic amplification of the electronic coupling of the redox cofactors and their immediate protein environment may be achieved via the temperature-dependent librational motion of the cofactors in their binding sites. This motion has to be tuned in such a way that its time constant becomes comparable with the inverse rate constant of the specific ET step, for example, for the reduction of Q_A in RCs of *R. sphaeroides*. Hence, to monitor the transients of

light-induced ET processes by time-resolved electron paramagnetic resonance (EPR), an appropriate matrix control is a prerequisite. By cooling the sample, $t_{1/2} = (k_{ET})^{-1}$ must be slowed down from the fast steps of the early ET events (subnanoseconds near room temperature) into the time window of transient EPR, which is restricted to about 10 ns upwards.

We have started a joint multifrequency EPR research project on site-specific mutants of *R. sphaeroides* to modulate, in a controlled fashion, the ET characteristics of cofactors in interaction with their RC protein environment. When applying high-field EPR methods for improving the spectral resolution of delocalized spin systems, in which unresolved hyperfine interactions dominate the inhomogeneous EPR line width, at least a lower limit of the microwave (mw) frequency and the corresponding B_0 field has to be fulfilled, which is defined by

$$\frac{\Delta g}{g_{iso}} B_0 > \Delta B_{1/2}^{hf} , \tag{1}$$

i.e., the anisotropic electron Zeeman interaction must exceed the inhomogeneous line broadening, $\Delta B_{1/2}^{hf}$. In this paper, we describe first results of high-field EPR spectroscopy at 95 and 360 GHz and of its double-resonance extensions ENDOR (electron–nuclear double resonance) [19] and PELDOR (pulsed electron–electron double resonance) [20] on frozen RC solutions. Taking advantage of the inherent capabilities of these spectroscopic techniques in terms of resolution and sensitivity, which go far beyond the capabilities of conventional X-band EPR spectroscopy, the subtle changes of the electronic and spatial structures of the redox-active cofactors upon mutation are elucidated. Specifically, mutation-induced changes of the local polarity, the H-bonding networks and the ligation of the axial magnesium atoms of the primary bacteriochlorophyll *a* donor special pair are monitored. As sensitive probes for mutation-induced changes of the protein–cofactor interactions we use *g*- and hyperfine tensor components as well as electron–electron dipolar interactions and anisotropic T_2 relaxation times. Whereas for the acceptor quinone radical anions, the *g*-tensor anisotropy is large enough to be resolvable by 95 GHz/3.5 T EPR, for the donor bacteriochlorophyll dimer radical cation, the *g*-tensor anisotropy is extremely small so that still higher Zeeman fields are required. For sufficient orientational Zeeman selection with resolved principal *g*-tensor components, 360 GHz/12.9 T EPR turned out to be well suited for frozen-solution samples. (A similar case of extremely small *g*-anisotropy is the flavin radical cofactor $FADH^{\bullet}$ in photolyase DNA repair enzymes [21, 22].)

2 Materials and Methods

2.1 RC Preparations (Wild Type, Mutants)

RCs of *R. sphaeroides* R-26.1 were isolated and purified according to methods described earlier with slight modifications [23]. The construction of the mu-

tants at position 202 in the M subunit, His → Glu HE(M202) and His → Leu HL(M202), has been described in refs. 24 and 16, respectively. The mutant RCs were prepared as described in ref. 25. Both mutations led to a loss of the Mg atom from the bacteriochlorophyll *a* (BChl) on the M side of the primary donor resulting in the formation of BChl-BPh "heterodimers". The buffers used for both mutants were 10 mM Tris-HCl at pH 8.0, 1 mM EDTA with 0.03% Triton X-100 as detergent. The buffer used for *R. sphaeroides* R-26.1 was 10 mM TrisHCl at pH 8.0, 1 mM EDTA with 0.03% polyoxyethylene-10-laurylether. The detergents utilized have been shown to prevent the formation of a different conformational state of the donor upon freezing of the sample [16]. The sample concentration was 0.2–0.3 mM. The samples were oxidized either by light-induced charge separation (λ = 785 nm) or chemically by adding 25 mM $K_3[Fe(CN)_6]$ (potassium ferricyanide) to obtain the primary donor radical cation $P^{\bullet+}$. The radical generation was controlled by monitoring the optical absorption band at 865 nm for the R-26.1 sample. Upon oxidation, the band decreased in amplitude but did not shift to lower wavelengths. For both HL(M202) and HE(M202), the chemical oxidation procedure was carried out under identical conditions. For 360 GHz EPR experiments, a sample volume of not larger than 1 µl was brought onto the gold-plated curved mirror of the resonator, transferred into the Fabry–Perot resonator at room temperature and then gradually cooled to 160 K.

The double mutant His → Glu at position L168/Asn → Asp at position L170, HE(L168)/ND(L170), has been obtained from N. W. Woodbury and J. P. Allen (Tempe, AZ, USA). It has first been described and characterized in ref. 26. This mutation introduces two protonable residues (Glu and Asp) in the vicinity of the primary donor. It furthermore breaks one of the hydrogen bonds between an amino acid (HisL168) and the acetyl keto group of P_L. The mutant was in 15 mM Tris-HCl, pH 8, 0.03% β-dodecyl maltoside, 1 mM EDTA, 150 mM NaCl, concentration of about 0.2 mM. For 360 GHz EPR experiments, the sample (sample volume, 10 µl) was oxidized on the curved gold-plated quartz mirror, which was then transferred into the precooled probehead.

To obtain narrow EPR signals from the quinone radical anions, $Q_A^{\bullet-}$ and $Q_B^{\bullet-}$, in bacterial RCs the high-spin nonheme Fe^{2+} ($S = 2$) was replaced by diamagnetic Zn^{2+} ($S = 0$) in *R. sphaeroides* R-26.1 following the procedure of Debus et al. [27].

Stable quinone radicals for the W-band ENDOR measurements were generated by illumination with a single, saturation laser flash. Excess cytochrome *c* was added to reduce the primary-donor radical cation after photooxidation. Due to the short duration of the laser flash (3 ns), multiple ETs within the same RC are suppressed, since the reduction of the donor radical $P_{865}^{\bullet+}$, a precondition for the ET to Q_B, occurs on a much slower time scale. Since Q_A is an intermediary acceptor, $Q_A^{\bullet-}$ is transient and only $Q_B^{\bullet-}$ is obtained. The quinone radicals can be distinguished either by their different g_{xx} values [28] or by differences in their hyperfine couplings (hfcs) [29, 30].

2.2 Density Functional Theory Methodologies

The quantum-chemical calculation of EPR parameters has experienced a tremendous step forward in the past few years by the progress in density functional theory (DFT). Parallel to this development, there has been an almost complete retreat of traditional semiempirical molecular orbital (MO) methods like INDO [31], AM1 [32] or ZINDO [33] from this area.

Various academic groups [34–41] have developed DFT computer program packages such as ADF [34, 36, 40] and ORCA [39]. In conjunction with the enormous progress in the computing power of common desk computers, they are efficient enough to allow quite reliable predictions of hyperfine and *g*-tensors within acceptable CPU times even for bioorganic molecules as large as the special pair P in bacterial and plant photosynthetic RCs.

Most DFT methods are based on the use of double perturbation theory starting from standard solutions of the nonrelativistic Kohn–Sham equations [34–39]. In the area of large biomolecules such as bacteriochlorophyll monomers and dimers, our research group at FU Berlin has made extensive use of the commercial Amsterdam Density Functional (ADF) program package developed by the theoretical chemistry groups in Amsterdam (E. J. Baerends and coworkers [42]) and in Calgary (T. Ziegler and coworkers [34, 35]). The DFT program package ORCA, made available by F. Neese (in Mülheim an der Ruhr, now in Bonn), has been preferably used by us for smaller systems, such as nitroxide spin labels, primarily for the study of polarity and hydrogen bond effects.

ADF can treat all elements of the periodic table and contains state-of-the-art relativistic methods and spin–orbit coupling to treat heavier atoms. Its quantum-mechanical/molecular-modeling implementation (QM/MM) enables the treatment of protein environments with many thousands of atoms. It includes the very latest meta-GGA and hybrid exchange-and-correlation functional. Specifically, our DFT calculations of *g*- and hyperfine tensors on the primary donors of the carotenoid-less wild type R-26.1 and its HL(M202) and HE(M202) mutants, which were studied experimentally by high-field EPR at 360 GHz [43] (see below), are based on the relativistic approach by Schreckenbach and Ziegler [34, 35]. This method is incorporated in the accompanying ADF Property Program Package (Release 2002). The calculations were performed at the "relativistic scalar Pauli" and spin-unrestricted level using double zeta (DZ) atomic basis sets built from Slater orbitals and the Becke exchange [44] and Lee–Yang–Parr correlation [45] options for the generalized gradient approach (GGA) part of the exchange-and-correlation (XC) functional.

The principal effects that dominate EPR spectra are obviously well accounted for by the currently available DFT methodologies. However, concerning the achieved quantitative accuracy of the *g*- and hyperfine tensors, there is still a significant lag behind the latest progress in the experimental methods. This has become particularly obvious from our recent experimental high-field EPR studies on bacterial primary donors (wild type and mutants), where the high-precision results of *g* shifts appear to be close to the borderline of the present ADF

capability. Nevertheless, significant momentum has been gained from such studies which should fertilize the development of improved theoretical methods for the quantum-chemical prediction of EPR parameters.

2.3 The 95 GHz Continuous-Wave/Pulsed EPR/ENDOR Spectrometer

As described in detail elsewhere [46–48], our 95 GHz (W-band) EPR/ENDOR spectrometer operates both in continuous-wave (cw) and pulsed mode at an external magnetic field of about 3.4 T for $g = 2$. A superconducting cryomagnet (Cryomagnetics, Oak Ridge, TE, USA; max. $B_0 = 6$ T; room-temperature bore diameter, 114 mm) provides the static Zeeman field, which can be swept for ± 0.1 T by controlling the current in additional superconducting sweep coils inside the magnet Dewar. The field-modulation coils for cw EPR experiments are part of the probehead and supply up to 1 mT at the sample at about 10 kHz. The heterodyne mw bridge works at an intermediate frequency (IF) of 4 GHz, which is provided by a dielectric-resonator oscillator (DRO). It allows convenient manipulation of phase and amplification. The 99 GHz local-oscillator signal is obtained by up-conversion of the 95 GHz signal oscillator power with the 4 GHz DRO. The 4 GHz power, resulting from down-conversion of the 99 GHz local-oscillator power and the power reflected from the EPR cavity, is amplified with a low-noise preamplifier and then quadrature down-mixed with the same 4 GHz DRO as local oscillator [49]. The resulting signal is guided either to a lock-in amplifier or, after optional further amplification, to a fast digitizing scope. The 95 GHz mw source uses four low-frequency oscillators, three fixed-frequency temperature-stabilized DROs and one voltage-controlled oscillator (VCO), operating at 7.3 GHz. The frequency of this mw field is further up-converted by a factor 13 using an IMPATT-active frequency multiplier. An additional gain of the 95 GHz power is obtained by a two-stage cw IMPATT amplifier in the transmitter channel. The output power of maximal +20 dBm (100 mW) allows to perform pulsed EPR experiments with $\pi/2$ pulse lengths below 30 ns. Also the cw performance of the EPR spectrometer has been further improved by means of the outstanding frequency stability (below 30 kHz per hour) and noise characteristics of the solid-state source (the amplitude noise is below -140 dBc/Hz at 10 kHz, the phase noise is below -100 dBc/Hz at 10 kHz).

Several different probehead configurations including Fabry–Perot resonators and TE_{011} cylindrical cavities have been designed and optimized for EPR or ENDOR experiments [49–53]. EPR experiments are typically performed with a probehead equipped with a TE_{011} optical transmission cavity (unloaded quality factor $Q_U = 5000$).

The ENDOR setup uses a slotted TE_{011} cylindrical cavity to reduce eddy currents induced by the radio-frequency (rf) field of the ENDOR coil, which is placed around the cavity [50]. For proton ENDOR the rf circuit is tuned to and matched for 140 MHz (with 40 MHz bandwidth) corresponding to the proton Larmor frequency at $B_0 = 3.4$ T. An rf power amplifier (Amplifier Research,

Souderton, PA, USA; Model 1000 LM8) of 300 W in cw and 2.5 kW in pulse mode is used. It yields 2–6 μs long rf π-pulses in proton ENDOR experiments. ENDOR on other nuclei can also be performed by using a short-cut rf circuit optimized for a central frequency of 40 MHz (with 30 MHz bandwidth).

For light excitation experiments either the pulsed Nd-YAG laser beam (355 nm, 532 nm wavelengths) or the cw light of a 100 W halogen lamp or diode laser (690 nm, 795 nm) is guided to the cavity by means of a quartz fiber with a diameter of 0.8 mm. Temperature control of the sample between 90 and 350 K is achieved by a stabilized nitrogen gas flow system in the probehead.

2.4 The 95 GHz PELDOR Setup

Additionally, the bridge is equipped with a fast (>50 ns) mw switch which allows to select between one of the three fixed-frequency DROs and the variable-frequency VCO operating around 7.3 GHz. It is placed in front of the frequency multiplier (×13) followed by an IMPATT power amplifier. The frequency operation range is determined by the bandwidth of the power amplifier and is 600 MHz around 95.0 GHz in our configuration.

The dual-frequency PELDOR experiment involves a three-pulse stimulated echo subsequence at frequency ν_1 (observer frequency) with a fixed pulse delay T between the second and the third pulse. The external magnetic field is fixed to a value B' (resonance field at frequency ν_1), and a pump pulse at the frequency ν_2 for the flip angle π of the partner spins is applied with a fixed delay time T' with respect to the second pulse of the observer sequence. The pump frequency ν_2 corresponds to the resonance field $B'' = B' + h(\nu_1 - \nu_2)/(g_e \cdot \mu_B)$ within the EPR spectrum of the partner radical. The values of ν_1 and ν_2 are monitored by measuring the frequencies of the low-frequency mw sources, the DRO and VCO, respectively. Their output frequencies of about 7.3 GHz are measured with a 1 kHz resolution of the frequency counter. This corresponds to a precision of 13 kHz at 95 GHz after multiplication of the low-frequency mw output by the factor 13.

Individual PELDOR signals are obtained by varying the interpulse delay τ of the three-pulse echo subsequence. At each τ value, distortion-free quadrature echo responses appear after phase cycling the first observer mw pulse $(+x,-x)$. These responses are consecutively measured for the pump pulse being switched on and off.

2.5 The 360 GHz cw EPR Spectrometer

The 360 GHz quasi-optical EPR spectrometer has been recently described in detail [48, 54]. The sources of the submillimeter mw bridge are two phase-locked W-band Gunn oscillators: a two times doubled 90.01 GHz oscillator (Radiometer Physics, Meckenheim, Germany), providing submillimeter radiation at $\nu = 360.04$

GHz for mw excitation of the sample, and a doubled 90.31 GHz local oscillator (Farran Technology, Cork, Ireland), which serves as the reference for the subharmonic down-conversion (bandwidth, 100 MHz) of the 360.04 GHz signal to an IF signal of 1.2 GHz. The submillimeter radiation propagates through a quasi-optical Gaussian beam transmission line consisting of off-axis elliptical mirrors and a corrugated wave guide to the probehead in the cryostat. Thereby standing waves in the spectrometer bridge can be largely avoided, and mw losses are reduced by about 20 dB, as compared to fundamental-mode or oversized waveguides as mw transmission lines.

Gaussian beam optics greatly facilitates an induction-mode design of the mw bridge with a bimodal resonator [55]. Even under imperfect matching conditions the induction-mode configuration discriminates the EPR signal from the excitation mw power (isolation of about 30 dB), which excites orthogonal degenerate resonator and transmission-line modes. B_0 fields up to 14 T (12.9 T for $g = 2$ systems) are provided by a Teslatron-H cryomagnet system (Oxford Instruments, Witney, UK) with an integrated superconducting sweep coil (sweep range of ± 0.1 T). The warm bore of the cryomagnet has a diameter of 88 mm. The static-flow cryostat (Oxford Instruments) of the spectrometer (inside diameter, 62 mm) supports sample temperatures between 4 K and room temperature. The probehead contains a semiconfocal Fabry–Perot resonator (unloaded $Q_U \approx 1000$), consisting of a free standing copper mesh that constitutes the flat mirror, and a spherical gold-coated quartz mirror.

In an alternative probehead configuration the copper mesh is removed, which reduces the spectrometer sensitivity by a factor of 40. To compensate the decreased sensitivity, the amount of sample has to be increased by the same factor. However, since the combination of low-noise mw components, an induction-mode detection scheme and a high resonant B_0 field of 12.9 T provides an excellent overall detection sensitivity, an increase of the necessary amount of sample from 0.5 µl (typical for an organic radical in 0.1 mM sample with resonator) to 20 µl (without resonator) is affordable for many samples. A quartz fiber integrated into the probehead allows for the generation of radicals or triplet states in the resonator by laser excitation.

2.6 The 360 GHz cw ENDOR Setup

The construction of very high-field EPR probeheads is aggravated by the very small dimensions of the submillimeter mw resonators. Even more demanding is the construction of ENDOR resonators in which the mw field B_1 has to be superimposed by a perpendicular rf field B_2, and consequently the resonator walls must have appropriate slots to be transparent for the rf [56, 57]. Heating effects due to rf losses in the resonator generally would limit the long-term stability of the spectrometer. The ratio of the rf power converted into heat and the incident rf power can be dramatically reduced by employing matched rf circuits [57]. Resonant circuits can generate the same rf field strength B_2 at the sample posi-

tion with reduced applied power, thereby problems with reflected rf power and standing waves can be avoided to large extent. In EPR/ENDOR spectrometers operating at B_0 fields below 4 T, the use of mw resonators is inevitable to achieve sufficient mw fields B_1 at the sample position. The magnitude of B_1 determines the spectrometer sensitivity and the possibility to saturate the EPR transitions. Microwave saturation is a necessary condition for cw ENDOR experiments. In a recent cw ENDOR study at 220 GHz/330 MHz, Maniero et al. showed [58] that proton ENDOR signals of nitroxide radicals in frozen solutions can be observed even without resonant cavity. This is due to the increased sensitivity and longer spin–lattice relaxation times at very high B_0 fields. Combining this no-resonator approach with the development of high-frequency rf circuits, we succeeded in the construction of a 360 GHz/550 MHz ENDOR setup for cw experiments.

Figure 2 shows the scheme of the resonant rf circuit together with a cross section and an exploded view of the 360 GHz EPR/ENDOR probehead. The sample is placed on the gold-coated quartz mirror and irradiated by an mw field B_1 and a perpendicular rf field B_2 that is provided by a single-loop ENDOR coil. The ENDOR coil is part of the resonant circuit (center frequency, 547 MHz; FWHM, 60 MHz) which can be frequency-tuned and impedance-matched by two trimmer capacitors close to the ENDOR coil. The rf power is provided by a digital frequency generator (Hewlett-Packard, Santa Clara, CA, USA; Model

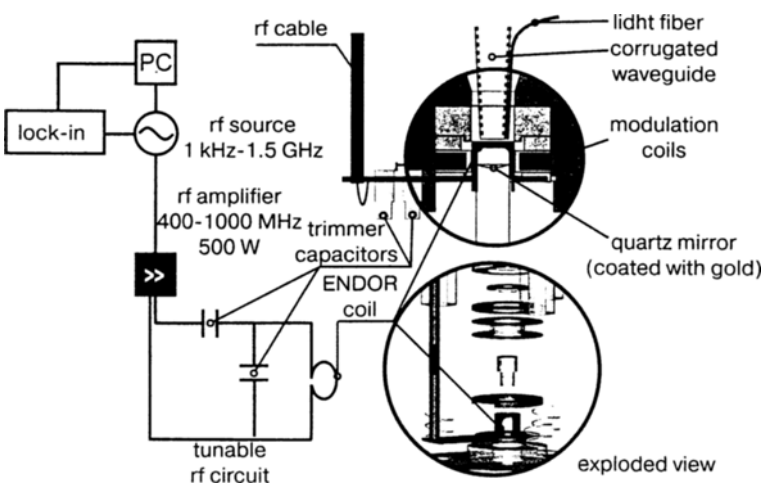

Fig. 2. Tunable rf circuit (left) together with a cross section and an exploded view of the 360 GHz/550 MHz EPR/ENDOR probehead (right). The resonant rf circuit consists of a single-loop coil and two trimmer capacitors, which provide frequency tuning and matching. The rf is generated by a sweepable generator, a power amplifier and a single-turn coil, which generates a B_2 field perpendicular to the mw field B_1. The sample is placed on the gold-coated spherical quartz mirror. Note that for this EPR/ENDOR experiment the mw coupling mesh as flat mirror of a Fabry–Perot resonator was removed. For details, see text.

8648B; 9 kHz–2 GHz) and amplified by a 500 W power amplifier (Amplifier Research, Souderton, PA, USA, Model 500 HB). To reduce standing waves in the rf transmission line, a high-power rf circulator is used. The maximum B_2 generated by the ENDOR coil is 0.8 mT at 20 W incident rf power, for which unwanted heating effects are avoided. ENDOR spectra are typically recorded at a fixed external field B_0 and mw field B_1, while sweeping the frequency of the rf field B_2. The latter is frequency modulated, and the ENDOR signals are recorded by using a lock-in amplifier.

3 Results and Discussion

3.1 360 GHz cw EPR on $P_{865}^{\bullet+}$, $Q_A^{\bullet-}$, $Q_B^{\bullet-}$ of RCs from R. sphaeroides

To start this section we refer to our earlier 95 GHz W-band EPR experiments on single crystals of RCs from *R. sphaeroides* R-26.1 at room temperature, both in their protonated and perdeuterated forms [51]. Owing to the high Zeeman resolution and narrow single-crystal line width, not only the magnetically inequivalent sites in the unit cell of the crystals could be resolved but also the full rotation patterns of their *g*-tensors recorded. From these patterns the principal directions of the *g*-tensors in the unit cell were determined. They reveal a breaking of the local C_2 symmetry in the electronic structure of $P_{865}^{\bullet+}$ which is consistent with the ENDOR/TRIPLE results for the hyperfine structure [59] (see below).

A striking result of these measurements on $P_{865}^{\bullet+}$ is a strong tilt of the *g*-tensor *z*-axis z_g (belonging to the smallest principal value g_{zz}) with respect to both planes of the two BChl monomers constituting the primary donor dimer. This was unexpected because at an inspection of the X-ray data [4], the π-electron systems of both BChl monomers appear to be planar in their major parts (the central macrocycles built from the four pyrrol rings) and, in this case, should yield the axis z_g practically parallel to the molecular out-of-plane *z*-axes. However, these measurements reveal that z_g is tilted against *z* by as much as 23°.

To get further insight into the origin of the observed tilt of the *g*-tensor *z*-axis with respect to an average molecular plane of the dimer, we employed ADF-DFT theory, paying closer attention to the behavior of the *g*-tensor principal axes in the two monomeric BChl moieties of the dimer. These calculations were performed on an energy-minimized monomeric BChl *a* model system containing all peripheral atomic groups, but excluding the phytyl chain (in total 82 atoms; computational details will be published elsewhere). The results of these computations can be summarized as follows. The energy-minimized structure has only a few local deviations of the central π-electron part from strict planarity, e.g., rotation of the acetyl group by 60° and puckering of the pyrrol rings I to IV by at most 4°. Nevertheless, the calculations yielded a tilt angle between the axes z_g and *z* of 32°. The direction of this tilt is roughly along a line connecting the atoms N_I and N_{III} of the respective pyrrol ring. This is close to what is observed for the $P_{865}^{\bullet+}$ dimer, where the spin density is mainly localized on the monomeric

half on the L side. Thus, the origin of the observed tilt g-tensor angle of $P_{865}^{\bullet+}$ is primarily traced to the nonplanarity of the L moiety of the dimer.

To further test this conclusion, we successively enforced increasing planarity of the model monomer structure in our calculations. In doing so, we found it necessary to cut off various peripheral atomic groups connected to the π-electron system by hyperconjugational coupling and to replace them by α-hydrogens sitting directly in the molecular plane. By this procedure we were able to reduce the tilt angle of the g-tensor z-axis to a value close to 0°, as would be expected. Interestingly, the in-plane enforcement of the acetyl group reduces the tilt angle only to about 17°, showing that this group is not solely responsible for the large tilt angle observed for $P_{865}^{\bullet+}$.

We thus conclude from these calculations that the observed tilt angle is a consequence of the broken C_2 symmetry of the special-pair electronic structure, but the symmetry breaking originates primarily in the nonplanarity of the individual BChl *a* monomer structures.

When turning from the RC single crystals to frozen-solution RC samples, as dictated by the nonavailability of RC single crystals of most mutant organisms studied in this work, the resolution of 95 GHz EPR is insufficient to resolve the extremely small g-tensor anisotropy of $P_{865}^{\bullet+}$. In this situation, 360 GHz EPR turned out to be essential for achieving sufficient orientation selection.

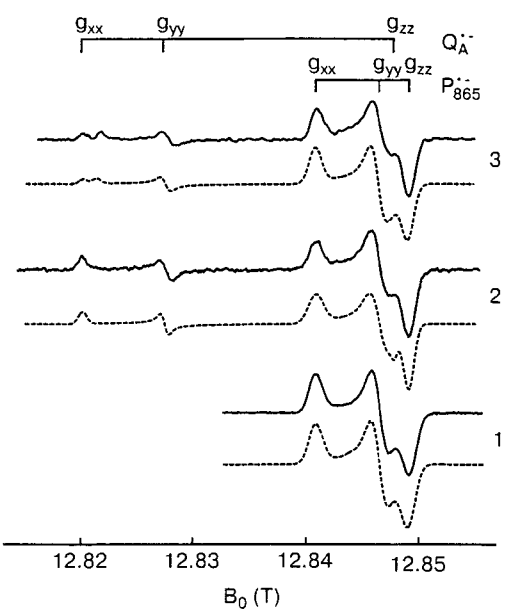

Fig. 3. Experimental (solid lines) and simulated (dashed lines) 360 GHz cw EPR spectra of the chemically oxidized bacteriochlorophyll $P_{865}^{\bullet+}$ (T = 140 K) (1), the light-generated radical pair $P_{865}^{\bullet+}Q_A^{\bullet-}$ (T = 140 K) (2), and light-generated radical pair $P_{865}^{\bullet+}Q_A^{\bullet-}$ together with a second quinone radical $Q^{\bullet-}$ (light excitation at 200 K, measurements at 140 K) (3). All measurements have been performed on Zn-substituted RCs from *R. sphaeroides*. For details see text.

Figure 3 shows, from bottom to top, the experimental (solid) and simulated (dashed) 360 GHz cw EPR spectra (1) of the chemically oxidized primary donor $P_{865}^{\bullet+}$ ($T = 140$ K), (2) of the light-generated (cw laser light at $\lambda = 785$ nm) radical pair $P_{865}^{\bullet+}Q_A^{\bullet-}$ ($T = 140$ K), and (3) of the same light-excited radical pair measured at 140 K, but after it had been photoexcited at $T = 200$ K. Spectra 2 and 3 had been measured under permanent cw-laser light excitation. When switching off the laser, the signal rapidly decays (lock-in time constant, 1 s). After a decay time of several minutes, the radicals can be again photogenerated, yielding the same spectra as observed initially.

As is seen from spectrum 3, photoexcitation at 200 K led to the appearance of a splitting of the g_{xx} component of the quinone spectrum, with the additional component shifted towards higher Zeeman field. Since the g-value of this spectral feature matches well with literature values of the g_{xx} component of quinone anion radicals [60], the splitting is assigned to a second quinone $Q^{\bullet-}$ overlapping with $Q_A^{\bullet-}$. Such a line splitting could originate from two different conformations of $Q_A^{\bullet-}$ present in the RC and trapped in the frozen protein matrix. It is well known that changes in the hydrogen-bonding network may alter the spin density distribution and thereby affect the g-values. This effect, however, would rather lead to a distribution of conformations with a broadening of the spectral components than to a discrete splitting. An alternative explanation for the observed splitting is a mixture of signals from primary and secondary electron acceptors $Q_A^{\bullet-}$ and $Q_B^{\bullet-}$ in the sample. To check this assumption, we performed spectral simulations, which included the known g-values of $Q_B^{\bullet-}$ [29]. The resulting simulation coincides well with the experimental spectrum. Hence, we assume that the observed high-field shifted peak in the quinone g_{xx} region originates from a fraction of $Q_B^{\bullet-}$ radicals generated in the photocycle. At temperatures well below 200 K, Q_B is trapped in its "dark" binding-site conformation and cannot accept electrons from $Q_A^{\bullet-}$ [4]. At higher temperatures, however, a fraction of the secondary quinone becomes part of the ET chain.

This finding nicely demonstrates the potential of very high field EPR to identify different radicals in a sample, even if they only slightly differ in their binding-site environment. Moreover, characterizing radical species via their g-tensor components and their dependence on inter- and intramolecular properties reveals much more information than just molecular fingerprints. Since the g-tensor represents a global probe of the electronic wave function of the species, information on the symmetry properties of the electronic structure may be extracted from precise measurements of g-tensor components. For organic radicals in frozen-solution samples the required accuracy of such measurements can only be achieved by sufficient Zeeman magnetoselection of the molecular orientation distribution, e.g., by very high frequency and high-field EPR such as at 360 GHz.

3.2 360 GHz cw EPR on $P_{865}^{\bullet+}$ of Mutant RCs from R. sphaeroides

The unidirectional nature of the primary ET route is probably not determined by a single structural feature but rather by the concerted effects of small contri-

butions of several different optimized factors affecting the energetics of the various intermediate states (the Franck–Condon factor F) and the coupling scheme of the cofactor wave functions (the electronic coupling matrix element V^2). Theoretical concepts invoke "overlap" and "superexchange" coupling mechanisms [8]. Both the wave functions and the energetics of the cofactors involved can be systematically changed by site-selectively exchanging neighboring amino acid residues of the protein environment by means of mutation (see Sect. 1). This can be accomplished, for instance, by introducing or disrupting H bonds of the cofactors or by changing the ligation of the Mg in the chlorophyll macrocycles of the primary donor P. In this context, it is particularly interesting to systematically study the influence of the environment of the primary donor, since P is generally considered to play a key role in the origin of the unidirectionality of the primary charge-separation steps [1, 16, 59, 61, 62].

The effect on the electronic structure caused by mutations can be measured, e.g., by transient absorption in the visible/near infrared regions [5, 6, 24] or via oxidation-potential changes [24, 63, 64] resulting in characteristic shifts of g-tensor and hyperfine tensor components that are resolved by high-field EPR [43, 51, 65] and ENDOR [16, 66–68], respectively. For example, in the course of X-band ENDOR and TRIPLE (electron–nuclear–nuclear triple resonance) [69] experiments on the R-26.1 mutant and wild-type RCs [1, 61, 62, 70], a pronounced asymmetry of 2:1 of the spin density distribution over the two dimer halves in $P_{865}^{\bullet+}$ was determined, favoring the BChl axially ligated by the L subunit. The electronic structure of $P_{865}^{\bullet+}$ in the R-26.1 mutant RC turned out to be similar to the carotenoid-containing wild-type RC [70]. In contrast, the asymmetry ratio was found to change drastically upon site-directed mutations near the primary donor [16, 67, 68]. The mutations were designed to add or remove hydrogen bonds between the acetyl and keto groups of P and histidine residues at symmetry-related sites of the protein. The changes in the hydrogen-bond situation of P were accompanied by considerable changes in the dimer oxidation midpoint potential [69] as well as in drastic changes of the spin density distribution over the dimer halves [16, 61]. The X-band ENDOR and TRIPLE experiments revealed that the addition or removal of hydrogen bonds gradually shifts the unpaired electron distribution from a predominant localization on the L half of the dimer to a strong localization on the M half, depending on the H-bond situation.

The ENDOR/TRIPLE experiments provide hfc's of the various magnetic nuclei in the $P^{\bullet+}$ molecule which represent local probes of the electronic wave function. The assignment of the individual hfcs to molecular positions is a difficult task. It involved selective isotope labeling and additional measurements on RC single crystals [57, 68]. A less time-consuming approach would be desirable to obtain information on the symmetry properties of the electronic structure. This is offered by g-tensor measurements. In contrast to the local hfc probes, the g-tensor represents a more global probe of the electronic wave function of the unpaired electron. For many bioorganic radicals, the g-tensor anisotropies Δg are very small and cannot be resolved by standard EPR at 9.5 GHz (X-band) or 35 GHz (Q-band), because the Zeeman-field shifts of the g-tensor components are

smaller than the inhomogeneous line width. $P_{865}^{+\cdot}$ in photosynthetic RCs exhibits extremely small g-tensor anisotropies of about 10^{-3}. It is, therefore, a prime example of a situation where even high-field EPR at 3.4 T/95 GHz can only partially resolve the powder pattern of disordered samples [51, 60, 65, 66, 72]. To move these samples into the high-field regime already at W-band frequencies, one has to reduce the line width by deuteration or to employ a single crystal for the measurements. In an attempt to determine, by means of the global g-tensor probe, the characteristic symmetry properties of the electronic structure of the primary donor, 95 GHz high-field EPR on illuminated single-crystal RCs of *R. sphaeroides* was performed at 12 °C, i.e., at physiological temperatures [51].

Even for protonated RCs, the single-crystal EPR line width is so small that at a field of 3.4 T the magnetically inequivalent sites in the unit cell of the RC crystal could be resolved. The rotation patterns of the RC single crystals, i.e., the angular dependence of their g-factors in the three symmetry planes of the crystal, have been measured and analyzed. The remarkable result is that the principal directions of the g-tensor are tilted in an average molecular axes system [51]. Thereby, a breaking of the local C_2 symmetry of the electronic structure of $P_{865}^{+\cdot}$ is revealed. This finding is consistent with the ENDOR/TRIPLE results for the hyperfine structure (see above).

To gain further insight into the origins and consequences of this asymmetry in the electronic structure, various site-directed mutants of the RC are being investigated in our laboratory at the FU Berlin by 360 GHz high-field EPR. In some of these mutants the ligands to the magnesium of the bacteriochlorophylls

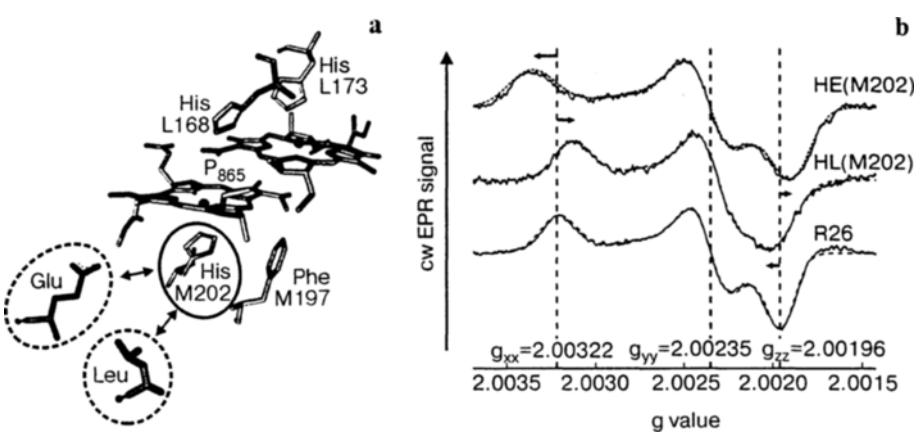

Fig. 4. a Site-specific replacement mutants of histidine M202 to glutamic acid and leucine, respectively. **b** 360 GHz cw EPR spectra (solid lines) of $P_{865}^{+\cdot}$ in RCs from the mutants HL(M202), HE(M202) and R-26.1 of *R. sphaeroides* at 160 K. The most prominent shifts of the g-tensor components g_{xx} and g_{zz} due to the mutations at M202 are indicated by horizontal arrows. Minimum least-squares fits for each spectrum are overlaid with dashed lines. The R-26.1 mutant can be considered as wild type with respect to the ET properties of the primary donor and acceptor. For details, see text.

were altered. Figure 4a shows the exchange of the histidine His(M202) by leucine (L) or glutamic acid (E) to generate the mutants HL(M202) and HE(M202), respectively. In the symmetry-related heterodimer mutants HL(M202) and HL(L173) [73], the His that ligates the Mg in the BChl is exchanged for a Leu. The leucine that does not ligate to the metal center results in a BChl:BPh heterodimer [74]. Owing to the large difference in the redox potentials of BChl and BPh (up to 300 meV in different solvents [75]), the mutation-induced changes of the ET characteristics of the heterodimer can be considered to be predominantly controlled by the energetics (Franck–Condon factor) when comparing it with $P_{865}^{\bullet+}$ of the native RC [6].

In HL(M202), the unpaired electron in $P^{\bullet+}$ was shown to reside on the BChl(L) [16, 73], in HL(L173) on the BChl(M) dimer half [73]. It was, however, also shown that in both mutants the main ET pathway is still along the A branch [76]. This finding indicates that the asymmetry in the electron spin density (and charge) distribution in $P^{\bullet+}$ is not a priori the major contributor to the unidirectionality of ET in bacterial RCs, but the conformational-gating effect is enhanced by specific cofactor–protein interactions along the active ET branch.

The expected shifts of the *g*-tensor components upon mutation will be extremely small – in the order of 10^{-4} – as has been shown by previous W-band measurements on similar mutants [65, 66]. The further increase of EPR frequency and B_0 field by a factor of 4 to 360 GHz and 12.9 T, however, provides the spectral resolution necessary to fully resolve all three principal *g*-tensor components of $P^{\bullet+}$ randomly oriented in frozen solution [77], and to measure their mutation-induced shifts [43] with high precision.

Figure 4b shows the 360 GHz EPR spectra of $P^{\bullet+}$ of *R. sphaeroides* R-26.1 in comparison with those of the HL(M202) and HE(M202) mutants [43]. Minimum least-squares fits to a model spin Hamiltonian including only the Zeeman interaction of radicals with an isotropic orientation distribution are shown as dashed lines together with the measured spectra. The *g*-values obtained from these fits [43] are in accordance with previous measurements within the error limits [51, 60, 65, 66, 72, 77, 78]. In discussing differences of *g*-values, such as $\Delta g = (g_{xx} - g_{zz})$, the error in the 360 GHz EPR measurements is only $2 \cdot 10^{-5}$, and the small shifts in the order of 10^{-4} that are induced by the mutations of the protein environment of $P^{\bullet+}$ are detected with high significance.

The *g*-component shifts observed in the 360 GHz EPR spectra are rather surprising. While for $P^{\bullet+}$ of HL(M202) the overall *g*-tensor anisotropy $\Delta g = (g_{xx} - g_{zz})$ becomes smaller than that for R-26.1, for HE(M202) Δg increases to a value considerably larger than that for R-26.1. This unexpected behavior of Δg strongly suggests a local structural change of BChl(L) as a consequence of the M202 ligand mutations.

Earlier semiempirical MO studies [79] and ENDOR/TRIPLE results on $P^{\bullet+}$ in RCs [16, 80, 81] suggest different torsional angles $\theta_{ac}(L)$ of the acetyl group of BChl with respect to the plane of the adjacent aromatic ring. Different values of $\theta_{ac}(L)$ for R-26.1, HL(M202) and HE(M202) are, in fact, expected in view of the different dimeric counterparts. This observation urged us to perform theo-

retical calculations of the g-tensors of the three $P^{\bullet+}$ species as a function of $\theta_{ac}(L)$. We have applied relativistic DFT methods employing the ADF package [42] and the SZ approach [34] for the calculation of magnetic resonance parameters. Details of the computations are given in our previous publication [43].

The essential conclusion from the current computations, which reproduce the experimental results quite well, is that a range of increasing angles $\theta_{ac}(L)$ between 0° and 35° is predicted. The increase in Δg in this series of mutants is entirely due to a decrease of g_{zz}. This is reasonable, since the tilt of the acetyl group perturbs the planarity of the electronic π-system and, therefore, primarily leads to changes in g_{zz}.

To model the experimentally observed strong shift of the g_{xx} component, one needs to take H-bonding interactions with the environment into account. An H bond of the acetyl-group oxygen atom to the neighboring histidine residue shifts g_{xx} to larger values, and we conclude that the strength of this H bond, i.e., the distance $r(H\cdots O_{ac})$, varies in the three mutant species according to $r(HE) < r(R\text{-}26.1) < r(HL)$. This conclusion cannot be tested directly by means of the X-ray structure because of its insufficient precision of the atomic positions. Further DFT calculations are in progress with the aim to gain a deeper insight into the general influence of polar amino acids as well as of superimposed electric fields and H-bond effects on the g-tensor components of photosynthetic cofactors.

We now turn to first 360 GHz cw EPR experiments on $P^{\bullet+}$ of novel double mutants of *R. sphaeroides* constructed with the aim to control the ET pathways in the RC. When studying the HE(L168)/ND(L170) double mutant by time-resolved transient absorption spectroscopy, Haffa et al. [9, 12] had made the intriguing observation that these mutations induce a pH- and excitation-wavelength-dependent switching of the ET pathway from the A to the B branch of the RC protein L and M domains (see above). Figure 5 shows 360 GHz cw spectra of

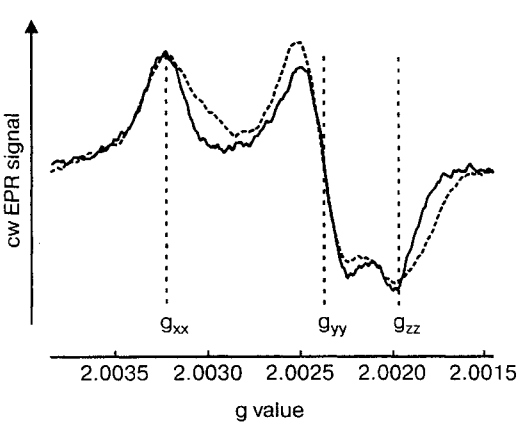

Fig. 5. 360 GHz cw EPR spectra of chemically oxidized $P_{865}^{\bullet+}$ in the wild-type RC (solid line) and in the HE(L168)/ND(L170) double-mutant (dashed line) RC from *R. sphaeroides* (pH 8, T = 160 K).

the chemically oxidized primary donor $P^{\bullet+}$ in the wild-type (solid line) and in the HE(L168)/ND(L170) double-mutant (dashed line) RCs from *R. sphaeroides* in frozen solution (pH 8, $T = 160$ K). Both spectra were recorded without resonant cavity. Simulations of the spectra yielded the principal g-tensor components $g_{xx} = 2.00325(5)$, $g_{yy} = 2.00240(5)$ and $g_{zz} = 2.00201(5)$ for the wild type and $g_{xx} = 2.00320(5)$, $g_{yy} = 2.00236(5)$ and $g_{zz} = 2.00198(5)$ for the double mutant. Within the experimental error of $\pm 5 \cdot 10^{-5}$ we found no difference in the g-tensor values, the main difference between the two spectra is an increased line width of the double mutant as compared with the wild type. The replacements of the histidine at position L168 by glutamic acid and the asparagine at position L170 by aspartic acid significantly lower the midpoint potential of the primary electron donor by -127 mV (pH 8) [26], as compared with the wild type. Since both the glutamic acid and the aspartic acid can be negatively charged in the protein environment, the change in the redox potential of P can be rationalized by the introduction of negative charges in the vicinity of the primary donor. Furthermore, the replacement of the histidine at position L168 by glutamic acid alters the hydrogen bond between the amino acid residue and the acetyl substituent of the BChl dimer. Changing the microenvironment in this way dramatically changes the ET characteristics of the RCs. This change in electronic structure is, however, not reflected by the g-tensor components of $P^{\bullet+}$ in the double mutant. Apparently, much more experimental and theoretical work needs to be done before the physical reasons for this observation are understood.

3.3 High-Field ENDOR

To extract information about the hfc's of a protein cofactor and, thereby, about its binding structure and spin density distribution, a combination of EPR and ENDOR proved to be the strategy of choice.

For a doublet radical, the ENDOR lines of a particular group j of equivalent nuclei with $I = 1/2$, appear, to first order, at

$$\nu^{\pm}_{j\mathrm{ENDOR}} = \left|\nu_{\mathrm{n}} \pm A_j/2\right| \tag{2}$$

with the nuclear Larmor frequency $\nu_{\mathrm{n}} = (g_{\mathrm{n}}\mu_{\mathrm{K}}/h)B_0$, where h is the Planck constant, μ_{K} is the nuclear magneton, and g_{n} are the nuclear g factors. The hfc values A_j contain isotropic and anisotropic contributions. In isotropic fluid solution, only the scalar values, 1/3Tr(**A**), are observed. In frozen solutions, powders or single crystals, on the other hand, also anisotropic tensor contributions become observable, provided appropriate spectral resolution conditions prevail.

The resolution enhancement of ENDOR versus EPR is particularly pronounced when nuclei or isotopes with different magnetic moments are involved. Their ENDOR lines appear in different frequency ranges, and by their Larmor frequencies these nuclei can be immediately identified. In the case of accidental overlap of ENDOR lines from different nuclei, however, by taking advantage of the

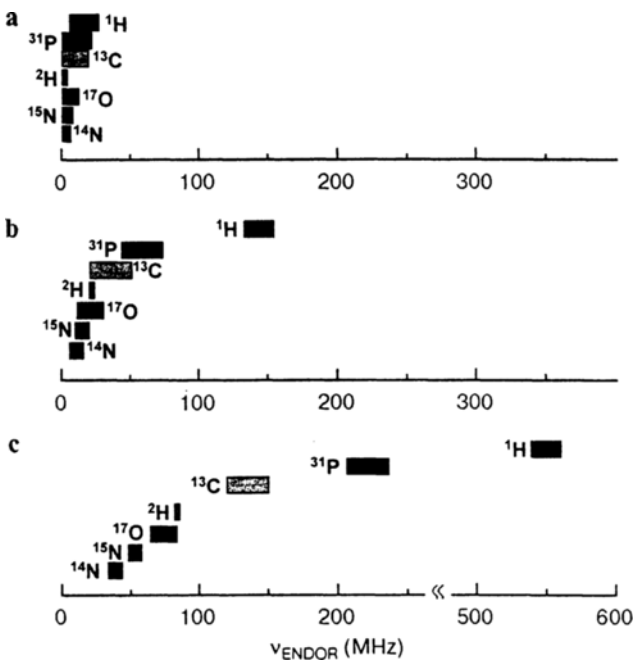

Fig. 6. Gain in ENDOR resolution for doublet-state ($g = 2$) systems with increasing Zeeman field and mw frequency: **a** $B_0 = 0.34$ T, $\nu_e = 9.5$ GHz, **b** $B_0 = 3.4$ T, $\nu_e = 95$ GHz, **c** $B_0 = 12.9$ T, $\nu_e = 360$ GHz. Spectral lines of different nuclei in organic biomolecules, largely overlapping at the traditional mw frequency of 9.5 GHz (X-band), start to separate at 95 GHz and become completely disentangled at 360 GHz.

field-dependent nuclear Larmor frequency, they can often be separated when working at higher Zeeman fields. If the molecule under study contains nuclei ($I > 1/2$) with a quadrupole moment, Eq. (2) is extended by a contribution $3/2(2m_I - 1)P$ (with $m_I = I, I - 1, \ldots \geq 0$) from the traceless nuclear quadrupole tensor, which splits or shifts the ENDOR lines provided the molecular system is in an anisotropic environment. P is a function of the quadrupole coupling constant, e^2qQ/h, the asymmetry parameter η, and the relative orientation of the quadrupole tensor with respect to the Zeeman field [82].

For large proteins the interpretation of ENDOR spectra is often hampered by overlapping resonant lines originating from different projections of the molecule and/or different nuclei and isotopes. Resulting ambiguities can often be clarified by means of high-field ENDOR experiments. High B_0 fields increase the spectral resolution in the ENDOR experiment in two ways as follows. Firstly, overlapping ENDOR spectra originating from different nuclei or isotopes may be disentangled by increasing the resonant field, since the Larmor frequencies are proportional to B_0, while the hfc's remain unchanged. This gain in ENDOR resolution is demonstrated in Fig. 6, which depicts typical extensions of ENDOR spectra in biomolecules, indicated by bars around the Larmor frequencies of dif-

ferent nuclei at Zeeman fields of 0.34, 3.4 and 12.9 T. At 0.34 T, the ENDOR lines of ^{1}H, ^{31}P, ^{13}C, ^{2}H, ^{17}O, ^{15}N and ^{14}N largely overlap. At 3.4 T, the Larmor frequency of ^{1}H is well separated from those of the other isotopes, but ENDOR spectra of ^{17}O and the nitrogen isotopes may still overlap. At 12.9 T, finally, all ENDOR spectra of the selected isotopes are nicely separated.

Secondly, high-field ENDOR has the additional advantage of providing single-crystal-like hyperfine information in the reference frame of the *g*-tensor, even from disordered molecules with very small *g*-anisotropy. The prerequisite for such an advantage is that the chosen Zeeman field B_0 is high enough for a pronounced magnetoselection of the different canonical orientations of the molecules.

3.3.1 95 GHz Pulsed ENDOR on $Q_B^{\bullet-}$ in ZnRCs from *R. sphaeroides*

The orientation-selection benefit of EPR at high B_0 is demonstrated in Fig. 7a. It shows the echo-detected W-band EPR spectrum of the secondary acceptor quinone $Q_B^{\bullet-}$ in RCs from *R. sphaeroides* in frozen solution at $T = 120$ K. The

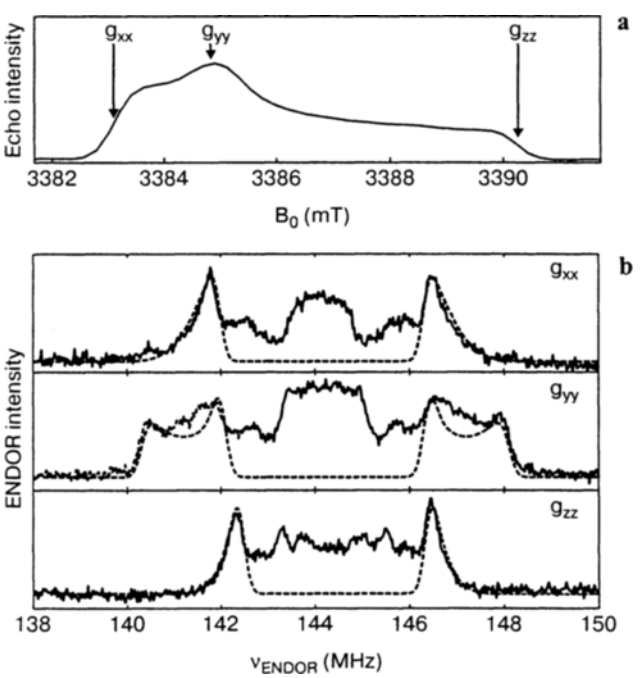

Fig. 7. **a** Echo-detected W-band powder EPR spectrum of $Q_B^{\bullet-}$ in frozen-solution RCs from *R. sphaeroides* ($T = 120$ K). The resonance positions of the principal *g*-tensor values g_{xx}, g_{yy} and g_{zz} are indicated by arrows. **b** W-band Davies-ENDOR spectra (solid lines) recorded at the g_{xx}, g_{yy} and g_{zz} positions of $Q_B^{\bullet-}$ in RCs from *R. sphaeroides* ($T = 120$ K). Dashed lines indicate the simulated (Easy Spin toolbox [103]) respective contribution of the methyl hfc to the ENDOR spectra. Note that the Larmor frequency and, thereby, the center of the ENDOR spectra increases proportional to the external magnetic field from g_{xx} to g_{zz}. For details, see text.

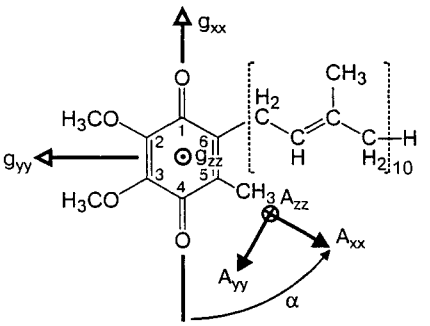

Fig. 8. Molecular structure and g- and methyl hyperfine-tensor axes systems of the ubiquinone-10 anion radical. The arrows indicate the canonical components of the molecular g-tensor and the methyl A-tensor, respectively, and α indicates the angle between g_{xx} and A_{xx}. The axes g_{zz} and A_{zz} are assumed to be collinear and oriented perpendicular to the molecular plane.

line shape exhibits the typical powder pattern of a well-resolved anisotropic g-tensor. The respective resonance positions of the principal g-tensor values are indicated by arrows. In this case of well resolved g-tensor components ENDOR measurements on defined spectral positions yield single-crystal-like information about the relative orientation of the hyperfine tensors with respect to the g-tensor. Thereby, the assignment of the hfc's are simplified and, even more important, valuable information about the orientation of the hyperfine tensor axes with respect to the molecular frame can be extracted.

This capability is demonstrated in Fig. 7b. It shows the Zeeman magneto-selection of W-band Davies-ENDOR spectra recorded at the canonical g-tensor positions of $Q_B^{\bullet-}$ ($T = 120$ K).

Pronounced orientation selectivity of the g-tensor, i.e., single-crystal-like ENDOR spectra, are expected at the g_{xx} and g_{zz} positions of the EPR spectrum, while in the center of the spectrum at g_{yy}, a broadened ENDOR spectrum is anticipated, as is indeed observed.

In Fig. 8 the orientation of the principal axes of the g-tensor and of the methyl hyperfine tensor of $Q_B^{\bullet-}$ with respect to the molecular frame are shown [29]. The g_{xx} component lies along the line connecting the two oxygen atoms, which carry most of the spin density; g_{zz} is perpendicular to the molecular plane and g_{yy} is perpendicular to both [83]. According to the extensive W-band ENDOR work on quinone radical anions by Rohrer et al. [49, 84, 85], the outer couplings in the range between 4 and 8 MHz can be assigned to the methyl group at position 5 (Fig. 8).

At a temperature of 140 K, methyl groups rotate almost freely about their C–C bond. Hence, the three hyperfine tensors of the individual protons of the methyl group in $Q_B^{\bullet-}$ collapse to only one hyperfine tensor, with the largest component A_{xx} oriented along the C–C bond [29, 85]. In the ENDOR spectrum taken at the position g_{zz}, only the A_{zz} component appears in the ENDOR spectrum, while at the resonance position of g_{yy}, both positions A_{xx} and A_{yy} contribute. A precise determination of the principal values and orientation of the methyl hyperfine

tensor with respect to the g-tensor and, thereby, to the molecular frame can be obtained by simulating the contribution of the methyl hfc's to the ENDOR spectra obtained at g_{xx}, g_{yy} and g_{zz}, respectively. The dashed lines in Fig. 7 show the results of the spectral simulations (the hfc's contributing to the central part of the ENDOR spectra have been excluded from the simulation). The following EPR and ENDOR parameter set was obtained from the simulations of the W-band Davies-ENDOR spectra of $Q_B^{\bullet-}$ in RCs from *R. sphaeroides*: $g_{xx} = 2.00626(5)$, $g_{yy} = 2.00527(5)$, $g_{zz} = 2.00210(5)$, $\alpha = 66(2)°$, $A_{xx} = 7.8(2)$ MHz, $A_{yy} = 4.4(2)$ MHz, $A_{zz} = 3.9(2)$ MHz. The angle α describes the in-plane deviation of the g- and hyperfine-tensor axes systems. The values obtained for the methyl hfc tensor of $Q_B^{\bullet-}$ by W-band Davies-ENDOR match nicely the results of cw Q-band measurements on $Q_B^{\bullet-}$ [29].

3.3.2 360 GHz cw ENDOR on the Test Sample DANO

Despite the success of the numerous W-band ENDOR studies since its introduction in 1988 [50, 86], there are many biological systems with several magnetic nuclei for which even higher magnetic fields B_0 are required to unambiguously analyze their ENDOR spectra (Fig. 6). Hence, to further increase their resolution, we developed a very high field ENDOR setup operating at an EPR resonance frequency of 360.04 GHz ($B_0 = 12.9$ T), corresponding to the free proton resonance at 547 MHz. Figure 9 shows the 360 GHz EPR (Fig. 9a) and ENDOR

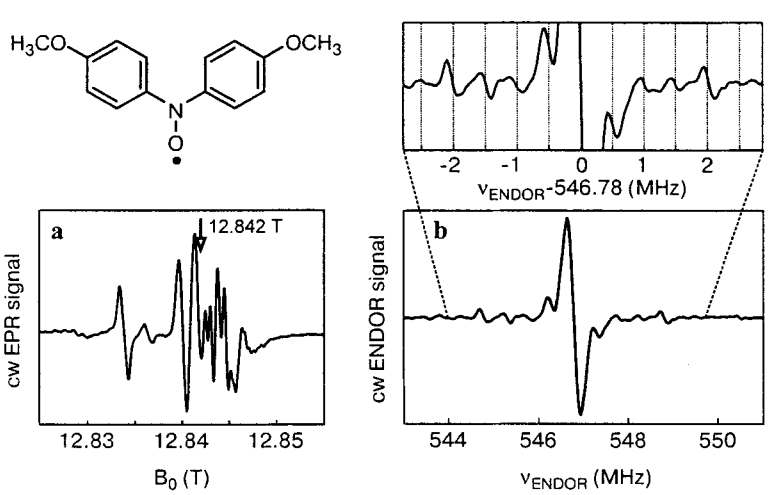

Fig. 9. **a** 360 GHz cw EPR spectrum of a polycrystalline DANO sample. Molecular structure of the di-anisyl nitric oxide (DANO) molecule. Experimental settings: $T = 100$ K; field-modulation amplitude, 0.5 mT; mw power, 0.05 mW at 360.04 GHz. The arrow indicates the spectral field position which has been fixed for the ENDOR experiment. **b** 547 MHz ENDOR spectrum of a polycrystalline DANO sample. Experimental settings: $T = 100$ K; frequency modulation deviation, 50 kHz at a modulation frequency of 100 kHz; mw power, 2 mW at 360.04 GHz; $B_0 = 12.842$ T.

(Fig. 9b) spectra of a polycrystalline nitroxide test sample (2% di-anisyl-nitroxide, DANO, in dimethoxy-benzophenone). The molecular structure of the DANO molecule is shown in Fig. 9. The EPR spectrum was measured at $T = 100$ K with a mw power of 0.2 mW at 360.04 GHz, omitting a resonant mw cavity. The external B_0 field was modulated (modulation amplitude, 0.25 mT at a frequency of 6.17 kHz).

Our polycrystalline DANO test sample exhibits a superposition of EPR spectra of nitroxide radicals in different orientations [50]. No efforts have been undertaken to interpret this EPR signal arising from several small crystals of unknown orientation with respect to the external magnetic field, which makes spectral simulations difficult.

The ENDOR spectrum shown in Fig. 9a was obtained at a resonant field of $B_0 = 12.842$ T. Saturation of the EPR signal was achieved by applying 2 mW of mw power at 360.04 GHz without using the mw resonator, i.e., removing the coupling mesh of the Fabry–Perot resonator (Fig. 2). The nuclear spin transitions of hyperfine coupled protons were driven by the additional B_2 rf field. By means of a computer-controlled frequency generator the rf was swept around $\nu_{rf} = 546.78$ MHz, which corresponds to the proton Larmor frequency at $B_0 = 12.842$ T. To increase the detection sensitivity, the rf field was frequency modulated (frequency, 100 kHz; deviation, 50 kHz) and the ENDOR response detected in a lock-in amplifier.

The ENDOR spectrum shows a 300 kHz broad resonance line centered at the proton Larmor frequency, it is attributed to many small unresolved hyperfine interactions with matrix protons. Furthermore, the ENDOR spectrum shows at least five resolved hyperfine lines symmetrically displayed around the proton Larmor frequency. For the same reasons as given above for the EPR spectrum of the DANO test sample, we refrain from interpreting the ENDOR signals. 360 GHz ENDOR experiments on protein samples are in progress. Particular attention will be given to resolving the quadrupolar contributions from ^{14}N and ^{2}H nuclei in nitroxide spin labels and deuterated hydrogen bonds, respectively.

3.4 95 GHz ESE-Detected EPR on the Spin-Correlated Radical Pair $P_{865}^{\bullet+}Q_A^{\bullet-}$ in ZnRCs from R. sphaeroides

In the following, we review our pulsed W-band high-field electron spin echo (ESE) experiments on the laser-pulse-generated short-lived $P_{865}^{\bullet+}Q_A^{\bullet-}$ radical pair in frozen RC solution of *R. sphaeroides* [87]. These experiments were performed with the aim to obtain, via spin polarization effects, information about the three-dimensional (3-D) structure of the charge-separated donor-acceptor system. This excited-state structure might differ from the ground-state structure, and, indeed, upon illumination of RC crystals of *R. sphaeroides*, drastic changes have been observed in the X-ray structure of the secondary quinone (Q_B) binding site in comparison with the dark-adapted RC X-ray structure [4]. The high-field EPR spectra were recorded using the field-swept two-pulse ESE technique. To avoid

fast spin relaxation of the $Q_A^{\bullet-}$, the nonheme Fe^{2+} ion was replaced by Zn^{2+}. The radical pairs $P_{865}^{\bullet+}Q_A^{\bullet-}$ were generated by 10 ns laser flashes ($\lambda = 532$ nm). Their time-resolved EPR spectrum is strongly electron-spin polarized because the transient RPs are instantaneously born in a spin-correlated noneigenstate of the spin Hamiltonian with pure singlet character. Such spin-polarized spectra with lines in enhanced absorption and emission originate from the SCRP (spin-correlated radical-pair) mechanism. Their line shapes contain important structural information of magnitude and orientation of the g-tensors of the two radical partners, $P_{865}^{\bullet+}$ and $Q_A^{\bullet-}$, with respect to each other and to the dipolar axis r_{QP} connecting the two radicals. Several parameters critically determine the line shape of the SCRP polarization pattern, such as the principal values and orientations of the g and electron dipolar-coupling tensors, the exchange coupling J, and the inhomogeneous line widths of both radicals [87].

From earlier time-resolved EPR measurements on $P_{865}^{\bullet+}Q_A^{\bullet-}$ at X-band (9.5 GHz), K-band (24 GHz) and Q-band (35 GHz), g-tensor orientations could not be extracted unambiguously from spectra simulations (for references, see ref. 88). This was caused mainly by strongly overlapping lines, even when deuterated samples were used to reduce hyperfine contributions. In the pulsed W-band ESE experiments, however, the Zeeman field is strong enough to largely separate the spectral contributions from $P_{865}^{\bullet+}$ and $Q_A^{\bullet-}$. The overall spectrum is dominated by the characteristics of the two g-tensors, and its interpretation is simplified. It enables an analysis of the tensor orientations. The most important result of this high-field ESE study is that, within error margins, no light-induced structural changes of Q_A with respect to P_{865} occur, as compared to the ground-state configuration $P_{865}Q_A$. This finding is in accordance with recent results from various other studies, including X-ray crystallography [4], and contrasts strongly with the Q_B situation. It is noted, however, that our recent PELDOR experiments reveal small, but significant conformational changes upon charge separation also for Q_A (see below).

3.5 95 GHz PELDOR on $P_{865}^{\bullet+}Q_A^{\bullet-}$

Light-induced transient radical pairs in photosynthetic RCs of plants and bacteria have been in the focus of numerous spectroscopic investigations over the past decades [89–92]. In particular, the charge-separated radical pairs $P^{\bullet+}Q^{\bullet-}$ of the primary electron donor and quinone acceptors have been characterized by a variety of time-resolved EPR methods in bacterial RCs, as well as in plant photosystem I and photosystem II. After pulsed laser excitation of the primary donor, $P^{\bullet+}Q^{\bullet-}$ appears in the SCRP state, which is characterized by a weak electron spin–spin coupling in a fixed geometry of the radicals in the pair and an initial singlet state of the system. The EPR responses of the SCRP display a number of interesting and useful spectroscopic features: spin polarization, quantum beats, transient nutations, as well as echo-envelope modulation and out-of-phase echo effects. From their analysis the magnetic interaction parameters and the geom-

etry of the system can be obtained. 3-D geometrical information about the radical pair is of particular importance. It allows to extract structural information about the transient charge-separated states in photosynthetic RCs for which only rarely [4] detailed X-ray data are available. Moreover, it allows to recognize and characterize the structural changes occurring in RCs upon charge-separation and charge-recombination processes. Although the time-resolved EPR signals of the SCRP are very sensitive to the relative orientation of the radicals in the pair, the number of parameters on which the SCRP line shape depends is large, and for unique solutions of the spectra simulations, additional independent information is needed. As a result, it is often difficult to judge the accuracy of the resulting pair geometry. Thus, an additional EPR methodology has to be developed which allows to obtain the orientation information directly, and this with predictable accuracy. This methodology is PELDOR spectroscopy on the SCRP at high magnetic fields. In the following we summarize the principles of the PELDOR spectroscopy on the SCPR in RCs, considering $P_{865}^{\bullet+}Q_A^{\bullet-}$ in a frozen solution of Zn-substituted *R. sphaeroides* R-26.1 as an example. We briefly describe the analysis of the SCRP spectra and, subsequently, the high-field PELDOR experiment. Finally, we discuss the extracted 3-D structure of the radical pair. A more extended description of high-field PELDOR experiments including the complete theoretical model and graphical analysis of the experimental data will be given elsewhere (A. Savitsky et al., unpubl.). It is noted that independent work of orientation-selective high-field PELDOR on large two-spin systems has been published very recently [93, 94].

For large interspin distances of well-localized electron spins in the radical partners, $P_{865}^{\bullet+}$ and $Q_A^{\bullet-}$, of a spin pair, for which the point-dipole approximation holds and the exchange coupling J can be neglected (as is often the case for the weakly coupled donor-acceptor radical pairs in photosynthesis), the electron-electron dipolar coupling frequency, ν_{QP}, is given by

$$\nu_{QP}(\theta) = \frac{\mu_0 \mu_B^2 g_P g_Q}{4\pi h} \cdot \frac{3\cos^2\theta - 1}{r_{QP}^3}. \tag{3}$$

Here, r_{QP} is the interspin distance in the radical pair and θ is the angle between the Zeeman field B_0 and the distance (dipolar) vector r_{QP} (Fig. 10a). The g-values $g_Q(\theta_Q,\varphi_Q)$ and $g_P(\theta_Q,\varphi_Q)$ refer to the radical pair oriented in the external field B_0, as is explained for $Q_A^{\bullet-}$ radical in the inset of Fig. 10a.

Figure 10b shows the EPR spectra of the individual radicals $P_{865}^{\bullet+}$ and $Q_A^{\bullet-}$ in frozen solution as calculated for X-band (9.5 GHz) and W-band (95 GHz) using the previously measured principal g-values $g_Q = [g_{xx}; g_{yy}; g_{zz}] = [2.00647; 2.00532; 2.00215]$ [83] and $g_P = [2.00325; 2.00234; 2.00196]$ [43]. At X-band the shape of the EPR spectra is governed by the inhomogeneous line width masking the canonical orientations. Thus, an isotropic distribution of angles θ is observed when probing the dipolar coupling between the radicals in the pair. Consequently, only a typical powder-type dipolar spectrum (Pake pattern) is obtained, from which the interradical distance r_{QP} can be determined, the orientational

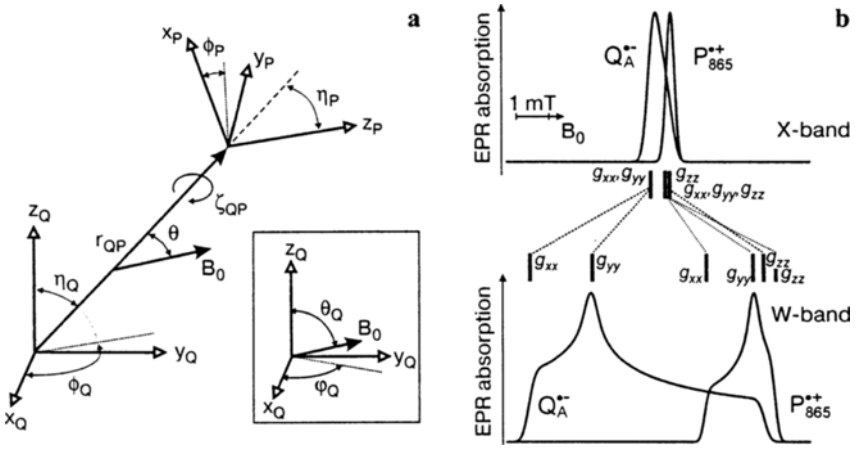

Fig. 10. **a** Geometrical representation of the respective g-tensor frames of R_Q (x_Q,y_Q,z_Q) and R_P (x_P,y_P,z_P) in terms of the polar angles η_Q, ϕ_Q and η_P, ϕ_P and the dipolar vector r_{QP}. The angle ζ_{QP} defines the relative tilt of the Q and P frames around the dipolar axis. The inset shows the g-value selection in Q-frame by the external magnetic field B_0. **b** Individual absorption EPR spectra of $P_{865}^{\bullet+}$ and $Q_A^{\bullet-}$ radicals as calculated for X-band (9.5 GHz) and W-band (95 GHz). The corresponding canonical g-values of both radicals are indicated. The individual spectra are normalized to the maximum amplitude. For details, see text.

information, however, is averaged out. In principle, it is possible to retrieve the orientational information by investigating the single crystals of RCs. In this case, certain pair orientations can be selected by rotating the single crystal in its symmetry planes with respect to the direction of B_0 [95]. Unfortunately, such single-crystal experiments and the subsequent data analysis of the rotation patterns are very time consuming. Thus, orientational information from disordered solids would be desirable. It is, of course, only available at a sufficient degree of orientation selectivity in the EPR powder spectrum by means of the anisotropy of a dominating spin-interaction parameter. For the radical pair $P_{865}^{\bullet+}Q_A^{\bullet-}$ this is the electronic g-tensor, which at sufficiently high magnetic fields provides the desired Zeeman magnetoselection. At W-band the condition for "real" high-field EPR, see Eq. (1), is fulfilled for $P_{865}^{\bullet+}Q_A^{\bullet-}$. The spectra appear with resolved canonical positions of the g-tensors of the respective radicals (Fig. 9b). Thus, if one can determine the dipolar frequencies at all resolved field positions within the EPR spectra of pair partners, i.e., selectively probing the electron dipolar coupling frequencies within the EPR spectrum of $P_{865}^{\bullet+}$ and $Q_A^{\bullet-}$, the full geometry of the radical pair can be reconstructed: the five angles η_Q, ϕ_Q, η_P, ϕ_P, ζ_{QP} and the interradical distance r_{QP} (Fig. 10a).

For SCRP systems in frozen isotropic solution the dipolar coupling frequencies at the canonical orientations of the g-tensors can be extracted from the spin-polarized EPR powder spectrum [96–98]. Photoexcitation of the primary RC donor leads to its excited singlet state, and this spin state is conserved during the ET because of the short lifetime of all intermediate states compared to the

time scale of all magnetic interactions. The radical pair $P_{865}^{\bullet+}Q_A^{\bullet-}$ is, thus, generated in a pure singlet state, $|S\rangle$. Because only two of the four eigenstates of the system contain admixtures of singlet character, the population of the energy levels of the SCRP is far away from thermal equilibrium. In the high-field limit, when the dipolar and the exchange interactions are small compared to the Zeeman interactions, the eigenstates of the four-level system of the radical pair can be approximated by the unperturbed triplet states $|T_+\rangle$, $|T_-\rangle$ and the mixtures of $|S\rangle$ and $|T_0\rangle$ states, as indicated in Fig. 11a by the energy levels 1, 4 and 2, 3, respectively. In each orientation of the radical pair with respect to the Zeeman field, one observes two pairs of EPR lines (antiphase doublets), corresponding to the four single-quantum transitions between the energy levels (Fig. 11a). They are equal in intensity, but one line appears in absorption (A), the other in emission (E). Both antiphase doublets are symmetrically positioned around the g factors of the individual partner radicals, $g_Q(\theta_Q,\varphi_Q)$ and $g_P(\theta_P,\varphi_P)$, orientation-selected by the B_0 field (Fig. 11b). The separation of each pair of lines is given by the dipolar coupling $-2d(\theta)$, if exchange interaction is neglected. Hence, the polarization pattern depends on the sign of the dipolar interaction. Inspection of Eq. (3) shows that at $\theta = 54.7°$ (magic angle) the dipolar coupling changes sign. Thus, E/A/E/A and A/E/A/E polarization patterns are observed for radical-pair orientations with $\theta < 54.7°$ and $\theta > 54.7°$, respectively (Fig. 10b). Consequently, it would be possible to construct the complete architecture of the radical pair from the rotation patterns of single-crystal high-field SCRP EPR spectra with sufficient spectral selectivity, because the dipolar frequency could be selectively

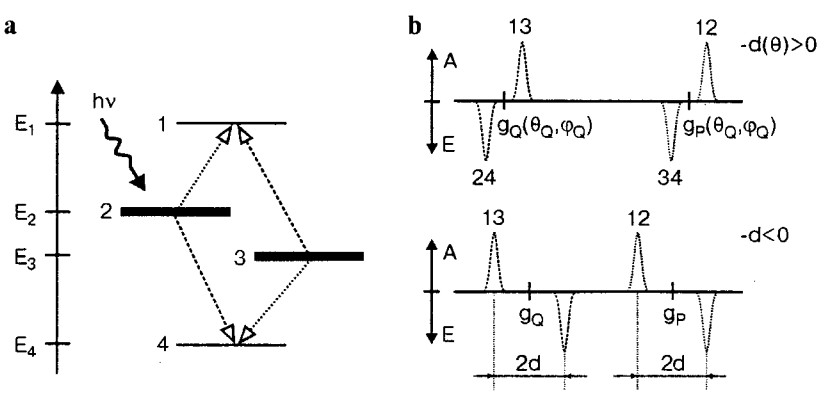

Fig. 11. **a** Energy level scheme for a coupled two-spin system formed in singlet state after light excitation. The arrows denote the single-quantum transitions between the energy levels. For the energy values and wave functions, see ref. 96. **b** EPR absorption spectra of the SCRP $P_{865}^{\bullet+}Q_A^{\bullet-}$ at a selected orientation with respect to the external magnetic field. The numbers on the EPR lines denote the transitions between the respective energy levels. The separation between the two line pairs is governed by the g difference between the radicals. The separation within the line pair is given by $-2d(\theta)$ (Eq. (4)), because the exchange interaction J is neglected. The top spectrum is observed for an orientation with negative $d(\theta)$, i.e., for $\theta < 54.7°$ (magic angle), the bottom one for a different orientation $\theta > 54.7°$ (positive $d(\theta)$). For details, see text.

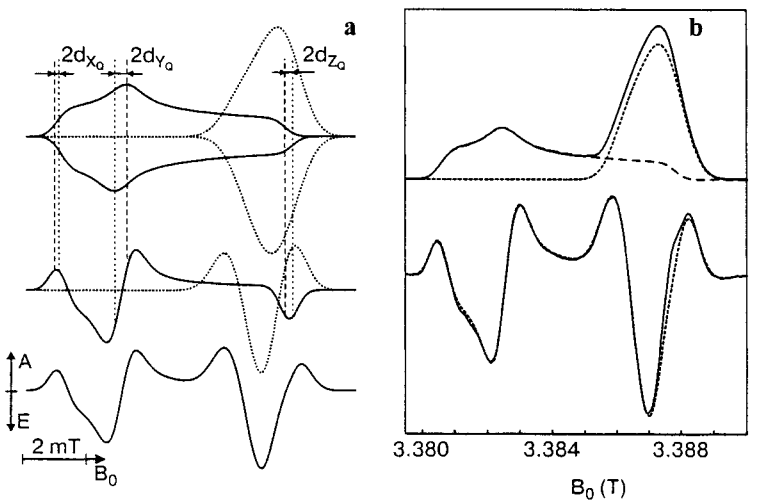

Fig. 12. a Calculated SCRP W-band EPR spectrum of randomly distributed $P_{865}^{\bullet+}Q_A^{\bullet-}$. Top spectra, the distribution of the four EPR lines in absorption and emission (solid lines for $Q_A^{\bullet-}$, dotted lines for $P_{865}^{\bullet+}$) as determined by the anisotropy of the *g*-tensors (Fig. 11a). Middle spectra, summation over corresponding absorptive and emissive contributions to the spectra of the individual radicals $P_{865}^{\bullet+}$ and $Q_A^{\bullet-}$ of the pair. Bottom spectrum, resulting EPR spectrum of the SCRP. The geometrical arrangement of the two cofactors from the Table 1 is used. For *g*-values and line width, see A. Savitsky et al. (unpubl.). A dipolar field of $d_0 = 0.15$ mT was used for this demonstration. **b** Field-swept two-pulse echo-detected W-band EPR spectra of $P_{865}^{\bullet+}Q_A^{\bullet-}$ in the Zn-substituted RCs from *R. sphaeroides* R-26.1 at 150 K for thermally equilibrated (top spectra) and SCRP (bottom spectra) states of the radical pair, taken at a delay-after-laser-flash time T_{DAF} of 500 μs and 200 ns, respectively. The signals from residual Fe^{2+}-containing RCs and the background steady-state signals are removed. The dashed lines give the calculated spectra, as described by A. Savitsky et al. (unpubl.). For the thermally equilibrated state (top spectra), the calculated spectra of $Q_A^{\bullet-}$ and $P_{865}^{\bullet+}$ are shown separately, by long and short dashes, respectively. For details, see text.

determined for any field position within the EPR spectrum of the pair. This single-crystal approach, however, would be very demanding in terms of experimental efforts and measuring time. In contrast, SCRP EPR spectra of frozen-solution samples are much easier and faster to record but have the disadvantage that they reflect only the powder average over all possible pair orientations. This averaging leads to a loss of information about the relative orientations of the partner radicals of the pair [99], i.e., the angle ζ_{QP} (Fig. 10a) cannot be obtained from frozen-solution spin-polarized SCRP EPR spectra alone. This is illustrated by Fig. 12a, which serves, in conjunction with a short excursion of SCRP theory, to explain the limited angular information content of EPR spectra of SCRPs in frozen solution, and how to overcome this limitation by additional PELDOR experiments on the same sample.

Figure 12a shows the formation principle of the EPR spectrum of SCRPs in randomly oriented RCs. At the top of Fig. 12a, the distribution of the four absorptive and emissive EPR lines from Fig. 11b is depicted, as determined by the respective anisotropy of the *g*-tensors of the $Q_A^{\bullet-}$ and $P_{865}^{\bullet+}$ radicals. The middle

spectra are obtained by summation over corresponding absorptive and emissive contributions to the spectra of the individual radicals. At the bottom of Fig. 12a, the resulting spectrum of the SCRP is shown. In the resulting SCRP spectrum the information about the orientation of corresponding g-frames relative to each other is averaged out. This means that after the powder averaging the contributions of SCRP spectra of the individual radicals can be considered to be independent. The spectral shape of the individual SCRP spectra depends only on the polar angles defining the distance vector (dipolar axis) in the corresponding g-tensor frame, i.e., η_Q, ϕ_Q in the $Q_A^{\bullet-}$ frame and η_P, ϕ_P in the $P_{865}^{\bullet+}$ frame. Characteristic derivative-like features are observed at the canonical positions of the g-tensor (Fig. 12a). The dipolar fields projected onto the canonical orientations of the g-tensor of $Q_A^{\bullet-}$, for example, are given by

$$\begin{aligned} d_{X_Q} &= d_0(1-3\sin^2\eta_Q\cos^2\phi_Q), \\ d_{Y_Q} &= d_0(1-3\sin^2\eta_Q\sin^2\phi_Q), \\ d_{Z_Q} &= -d_{X_Q} - d_{Y_Q} = d_0(1-3\cos^2\eta_Q), \end{aligned} \tag{4}$$

where $d_0 = [h\nu_{QP}(\theta = 90°)]/(\mu_B g_e)$ is the canonical dipolar field when approximating $g_Q \cong g_P \cong g_e = 2.0023$. Thus, the angle ζ_{QP}, which defines the relative tilt of the Q and P frames around the dipolar axis, cannot be obtained from the powder-averaged SCRP spectrum. Moreover, the d_Z values for the $P_{865}^{\bullet+}$ and $Q_A^{\bullet-}$ radicals cannot be measured precisely from the SCRP spectrum due to the close proximity of the g_{zz} values. Thus, the full equation system, combining Eq. (4) for $P_{865}^{\bullet+}$ and $Q_A^{\bullet-}$, becomes underdetermined, i.e., there are only four equations for five independent parameters. Additionally, the experimental SCRP spectrum contains an unknown scaling factor of the spectral intensities, which does not allow to use the dipolar parameter d_0 obtained from independent experiments [100]. This problem can be solved by scaling the SCRP spectrum to the EPR spectrum of the radical pairs in the same sample after their thermal equilibration [99], thereby providing the needed correlations for the polar angles. Figure 12b depicts the experimental EPR spectra of $P_{865}^{\bullet+}Q_A^{\bullet-}$ radical pairs in their spin-correlated and thermally equilibrated states, i.e., when recording the EPR spectra at 200 ns and 500 µs, respectively, after the laser flash. The simultaneous fit of both spectra allows to determine the following correlations for the polar angles η_Q, ϕ_Q for $Q_A^{\bullet-}$:

$$\begin{aligned} d_{Y_Q}/d_{X_Q} &= \frac{1-3\sin^2\eta_Q\sin^2\phi_Q}{1-3\sin^2\eta_Q\cos^2\phi_Q} = -2.90, \\ d_{X_Q}/d_0 &= 1-3\sin^2\eta_Q\cos^2\phi_Q = 0.46 \end{aligned}$$

and the corresponding values of −1.25 and 0.95 for $P_{865}^{\bullet+}$. The solution of these correlations yields several sets of possible polar angles. We choose the following set for further considerations: $[\eta_Q, \phi_Q, \eta_P, \phi_P] = [244.3°, 102.5°, 59.5°, 81.5°]$;

the dipolar vector is assumed to be directed from the Q to the P frame (Fig. 10a). It is important to emphasize that the accuracy of this set of angles is difficult to estimate because the simulation of the EPR spectra requires also additional input data, such as exact g-tensor values and orientation-dependent line width parameters.

Thus, only four angular parameters can be extracted from the analysis of SCRP spectra of $P_{865}^{\bullet+}Q_A^{\bullet-}$ in frozen-solution RCs because the fifth angle, ζ_{QP}, is averaged out in the powder spectrum of the interacting radicals. This tilt angle as well as independent proof of the preliminary polar angular parameters extracted from the SCRP spectra can be determined by spectrally selective PELDOR [101]. The PELDOR technique simultaneously uses two mw fields with different frequencies employing selective pulsed mw excitation within the EPR spectra of both interacting radicals. Thereby, PELDOR measures directly the dipolar coupling frequency, Eq. (3). Figure 13 shows the mw pulse scheme for dual-frequency PELDOR on pulsed laser-generated SCRPs. Within the mixing period between the three-pulse stimulated echo pulses, which are frequency-adjusted (ν_1) to an EPR transition of the observer spins (either $Q_A^{\bullet-}$ or $P_{865}^{\bullet+}$), an additional mw π-pulse in resonance (at ν_2) with the partner spins is applied to flip them. The two frequencies ν_1 and ν_2 for the observer spins and partner spins, respectively, correspond to the two Zeeman resonance fields B'' and B' (Fig. 13), which are interrelated by $B'' = B' + h(\nu_1 - \nu_2)/(g_e\mu_B)$. This allows to reverse the sign of the dipolar interaction field during the preparation (time τ between first and the second $\pi/2$ mw pulse of the observer sequence) and the detection (time τ between third $\pi/2$ pulsed and spin-echo formation). As the result, the echo responses in dependence on τ become amplitude modulated with the frequency of the dipolar interaction, Eq. (3). For the SCRP state two echo responses are formed, the in-phase signal S_{-y} and the out-of-phase signal S_x [101]. It is often advantageous to use the out-of-phase responses of SCRP. They are amplitude enhanced as compared to in-phase echoes, especially in the spectral regions where

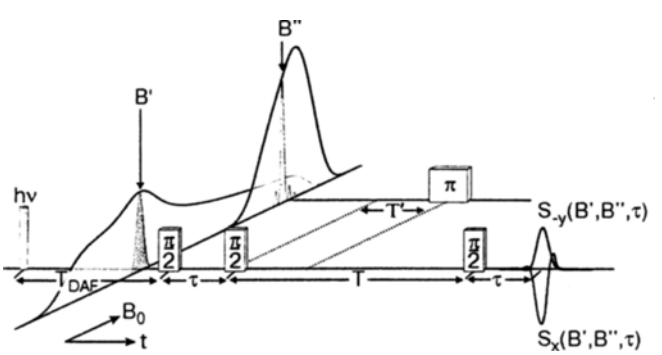

Fig. 13. Pulse sequence of the dual-frequency W-band PELDOR experiment on laser pulse-generated SCRPs with in-phase (S_{-y}) and out-of-phase (S_x) echo detection. The thermally equilibrated EPR spectra of both radicals, $P_{865}^{\bullet+}$ and $Q_A^{\bullet-}$, as well as the mw excitation bandwidths for typical mw pulse-length settings are shown for clarity. For details, see text.

the in-phase amplitude of the SCRP signal approaches zero (Fig. 12). Additionally, the out-of-phase echoes are amplitude modulated by $\sin(2\pi\nu_{QP}\tau)$, whereas the modulation of in-phase echo signals shows cosine behavior. Figure 13 holds for one specific data point of the PELDOR experiment. The complete PELDOR data surfaces are obtained by taking the echo signals at different positions of B'' within the partner EPR spectrum, i.e., by stepping the mw frequency ν_2 in typically 5.6 MHz (corresponding to 0.2 mT) steps. Thereby the PELDOR spectra of only those radicals $P_{865}^{\bullet+}$ and $Q_A^{\bullet-}$, which are conjugated by dipolar cross-talk, are detected. In principle, they contain information about the geometry of the radical pair, which is encoded in the characteristic modulations of the echo amplitude.

The specific conditions to be fulfilled for such a double magnetoselection provide the needed correlations between those angular parameters that complete the determination of the full pair structure. As stated above, this is not possible from the analysis of SCRP spectra alone. The experimental procedure for determining the full pair structure was as follows. In a first step, the B' and B'' positions were located where both radicals of the pair are coupled by the "parallel" dipolar frequency, $\nu_{QP}(\theta = 0)$, i.e., at first $g_Q(\eta_Q,\phi_Q)$ and $g_P(\eta_P,\phi_P)$ were determined. Geometrical consideration of these spectral positions together with the angular correlations obtained from the analysis of the SCRP spectra give precise polar angles: $\eta_Q = 109.5\pm2°$; $\phi_Q = 242\pm2°$; $\eta_P = 59\pm2°$; $\phi_Q = 82\pm2°$ (A. Savitsky et al., unpubl.) As soon as the orientation of the dipolar vector in each radical frame is known, PELDOR experiments were performed to find the spectral field positions at which only the "perpendicular" cross-talk dipolar frequency, $\nu_{QP}(\theta = 90°)$, can be detected. The analysis of these positions yields, as possible options, four allowed ζ_{QP} tilt angles of the pair: 50°, 120°, 230° or 300°. To choose between them, in a final step the analysis of the PELDOR responses in noncanonical dipolar positions was performed, which fixes the tilt angle to $\zeta_{QP} = 50\pm2°$. Additionally, an interradical distance of 2.94 ± 0.03 nm is calculated from the "parallel" and "perpendicular" dipolar frequencies of about 2.05 and 4.1 MHz, respectively. The exchange interaction was found to be negligible.

The solution of the geometry of the $P_{865}^{\bullet+}Q_A^{\bullet-}$ radical pair found by high-field PELDOR should be compared with the structure of a model ground-state reference pair $P_{865}Q_A$. The radical ions $P_{865}^{\bullet+}$ and $Q_A^{\bullet-}$ are assumed to stay at the same binding-site positions as their precursor cofactors, P_{865} and Q_A, in the dark-state RC. These positions were determined previously [4] (Brookhaven PDB entry 1AIJ) by X-ray crystallography. To describe the relative positions of the radicals within the reference pair in the same terms of distance and angle parameters, the reference Q_{ref} and P_{ref} frames were attached to the cofactor coordinates as determined from X-ray crystallography. For $Q_A^{\bullet-}$, the principal x-axis of the g-tensor was aligned to be collinear with the averaged director of the C_4–O_4 and C_1–O_1 bonds of ubiquinone-10 (Fig. 8). The y-axis was aligned perpendicular to the x-axis in the averaged plane of the quinone ring. The z-axis was taken to be perpendicular to both x and y, i.e., normal to the quinone plane. The origin of

Table 1. Angular parameters and distance describing the geometry of the $P_{865}Q_A$ pair. The angles are given for the transition from the Q frame to the P frame, i.e., the dipolar vector direction is Q-P.

$P_{865}Q_A$ pair	η_Q (°)	ϕ_Q (°)	η_P (°)	ϕ_P (°)	ζ_{QP} (°)	r (nm)
Reference pair[a]	97.4	246.2	66.2	79.5	49.5	2.84
PELDOR radical pair[b]	109.5	242	59	82	50	2.94

[a] Reference pair: obtained from X-ray crystallographic data [4] (PDB entry 1AIJ) of the dark state RC completed by the W-band EPR single crystal investigation of $P_{865}^{\bullet+}$ [51].
[b] PELDOR radical pair: obtained from ESE-detected W-band EPR combined with PELDOR.

the Q_{ref} frame was set at the center of the quinone ring. This approximates the electron spin-density center of the radical. The chosen attachment of the axes system is common for quinone molecules and follows from their symmetry. The alignment of the $P_{865}^{\bullet+}$ g-tensor (P_{ref} frame) within the primary donor was calculated on the basis of the results of the previous W-band cw EPR study on single crystals of *R. sphaeroides* R-26.1 [51]. From this study, the principal axes system (g_2), which was confirmed by pulsed W-band EPR experiments [87], was chosen also for our present work. The origin of the P_{ref} frame was positioned at the electron spin-density center of $P_{865}^{\bullet+}$. This position was obtained by projecting the coordinates of the spin-density center of the primary-donor special pair (82-atom $BChl_L$, 82-atom $BChl_M$), as determined from DFT calculations, onto the X-ray structure [43]. The coordinates of the heavy nitrogen and magnesium atoms of the bacteriochlorophylls were used to adjust the structures of primary donor of the reference, P_{865}, and the radical, $P_{865}^{\bullet+}$, molecules. Evaluation of the reference-pair configuration yields the angles and distance listed in Table 1.

Some parameters evaluated for the reference pair differ from those derived in our PELDOR study, and some differences exceed the error margins specified for both parameter sets, whereas other parameters agree very well. The discrepancies indicate that several of the assumptions and approximations made for simplifying the characterization of the reference pair in the g-frames should be revised. One might argue that setting the frame origins at the spin-density centers of the radicals is not exact, considering the fact that the point-dipole approximation of the dipolar interaction between spins is violated when the spins are delocalized over the rather extended orbitals of the radicals $P_{865}^{\bullet+}$ and $Q_A^{\bullet-}$. However, our calculations accounting for this delocalization did not significantly correct the positions of representative point dipoles and did increase the X-ray structure-derived distance r_{ref} only by 0.02 nm. Thus, we conclude that the difference between the two distance evaluations, $\Delta r = r_{QP} - r_{ref} = 0.08$ nm, has been reliably detected by our PELDOR experiments, i.e., that the Q_A–P_{865} distance between the ground-state ("dark") and the charge-separated state ("light") structures differs by a significant amount.

To change the pair distance upon charge separation, some displacement of any of the cofactors in their transient ion-radical states from their dark-state

positions must occur. Such a displacement is more probable for the smaller quinone than for the large special-pair primary donor and should be less restricted by the surrounding protein scaffold. In an attempt to visualize the difference between the parameter sets compared in Table 1 by drawing the displacement of the quinone after photoinduced ET, while the donor remains at a fixed position, we plotted the PELDOR-derived pair structure in Fig. 14 and overlaid it with the X-ray reference pair with both P frames coinciding. The resulting position of the Q-frame origin was found to be shifted from the Q_{ref}-frame origin by 0.39 nm, which, at a first glance, looks unrealistically large. However, this shift is directed mostly tangentially to the dipolar axis. Considered from the P_{ref} frame, the dipolar axis, when following the tangential shift of the Q origin, is tilted from its reference direction by 7.5°. Supposing a reasonable tangential shift to be of the same order as the observed longitudinal displacements of Q_A, i.e., less than 0.1 nm, the excursion of the dipolar axis would be less than 2°. Excursions as large as 5.5° are within the error margins when specified for the joint evaluation of the directions of r_{QP} and r_{ref} (Fig. 14). We note that angular PELDOR measurements for $P_{865}^{\bullet+}$ suffer from its extremely small g anisotropy and, thus, low Zeeman orientation selectivity. This might be improved by further increasing

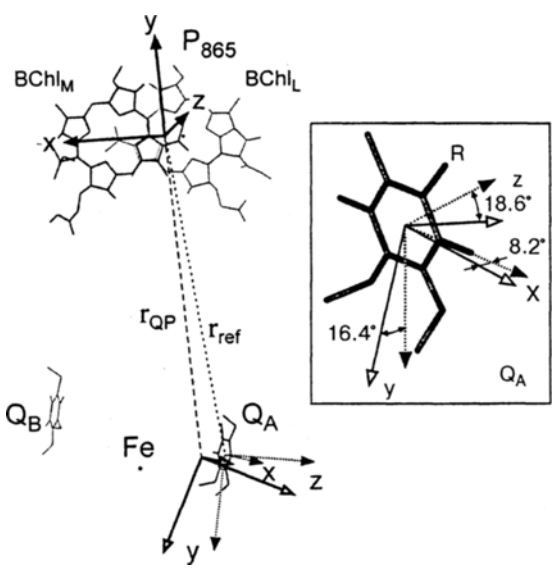

Fig. 14. PELDOR-derived (solid axes with open arrowheads) structure of the $P_{865}^{\bullet+}Q_A^{\bullet-}$ radical pair in the RC from *R. sphaeroides* overlaid with a reference structure (dotted axes with filled arrowheads) derived from X-ray data [4] (PDB entry 1AIJ) and $P_{865}^{\bullet+}$ single-crystal W-band EPR [51]. For the primary donor the P-axes of both structures were chosen to coincide. The inset visualizes the angular difference of the PELDOR and reference frames of $Q_A^{\bullet-}$ where the PELDOR frame has been translated to the geometrical center of the Q_A cofactor. R stands for the phytyl chain of Q_A. For details, see text.

the Zeeman B_0 field and by H–D substitution within the donor moiety. Such experiments, supported by quantum-mechanical calculations, are in progress.

Finally, we compare the Q frames, as obtained from ESE-detected EPR and PELDOR at W-band, with the constructed reference frame. The inset of Fig. 14 shows both frames with the EPR frame translated to the origin of the reference frame. The mismatching angles between the corresponding Q-frame axes are determined to be [8°, 16°, 19°]. Moreover, the transition from the reference frame to the EPR frame can be achieved by a first rotation by 14° around the x-axis, followed by an 8° rotation around the y-axis of the reference frame. The last rotation angle is within the error margins of the joint frame evaluation, i.e., the errors of the X-ray structure, the orientation of the P_{ref} frame from single-crystal EPR measurements [51] and the overall accuracy of the ESE-detected EPR and PELDOR experiments. The rotation angle around the x-axis lies clearly outside of this error margins. This deviation may be explained by a small reorientation ($<10°$) of the quinone cofactor around its molecular x-axis as a consequence of the charge-separation process. This explanation is in accordance with earlier investigations of librational dynamics of $Q_A^{\bullet-}$ [84, 102] at temperatures around 150 K. At these temperatures also our experiments were performed. The analysis the T_2 relaxation anisotropy of $Q_A^{\bullet-}$, as observed by W-band ESE-detected pulsed EPR [84, 102], shows that the quinone molecule performs anisotropic fluctuations. At temperatures below 160 K, the fluctuation axis lies along the dominant H-bond directions to the histidine and alanine amino acids of the Q_A binding site, i.e., the librations occur around the x-axis of the quinone molecule. An rms fluctuation angle of 24° around the x-axis of the $Q_A^{\bullet-}$ g-tensor was found at 140 K. However, a librational deviation of the x-axis from its mean position by only 12° was determined [102]. This observation indicates that $Q_A^{\bullet-}$ in its protein binding pocket does not experience too severe constraints to allow for such librational excursions. Hence, an equilibrium reorientation of Q_A upon charge separation by about 10°, as deduced from our PELDOR experiments, appears to be quite reasonable and may have escaped detection by other methods [4]. As expected from the X-ray structure, the observed light-induced reorientation of Q_A is indeed very small compared with the dramatic changes the Q_B binding site experiences under light excitation [4]. To prove the supposition of Q_A reorientation, the dipolar EPR experiments have to be extended to lower temperatures at which the $Q_A^{\bullet-}$ cofactor is well stabilized by strong H bonds [29]. Such experiments are in progress.

4 Conclusions

In this contribution it is shown that multifrequency high-field EPR, ENDOR and PELDOR studies are very promising for a better understanding of subtle interactions between the ET cofactors and their surrounding protein matrix. These interactions tune the electron distributions (electronic coupling matrix elements) as well as the energetics and dynamics (Franck–Condon factor) for optimized

photosynthetic ET. Multifrequency EPR spectroscopy, in particular at high magnetic fields, provides detailed information about structure, dynamics and spin chemistry of transient radicals and radical pairs occurring in the photochemical reaction cycle.

Since many organic cofactors in proteins have only small *g*-anisotropies, much higher magnetic fields than available at X-band are needed to resolve the canonical *g*-tensor orientations in the powder spectra. Thereby, even on disordered samples, orientation-selective hydrogen bonding and polar interactions in the protein binding sites can be traced. Whereas quinone radical anions (and nitroxide spin labels) exhibit *g*-tensor anisotropies that can be resolved by 95 GHz EPR, (bacterio)chlorophyll radical cations and neutral flavin radicals, as prototypes for extremely small *g*-anisotropy, require still higher Zeeman fields, for example, EPR at 360 GHz/12.9 T. In ET processes often several organic radical species are generated as transient intermediates. To distinguish them by the small differences in their *g*-factor and hyperfine interactions, high Zeeman fields are required and, hence, high-frequency EPR becomes the method of choice. Often high-purity protein samples can be prepared only in minute quantities, for example, site-directed mutants or isotopically labeled cofactors. Accordingly, to study them by EPR, very high detection sensitivity is needed, which often can be accomplished only by dedicated high-field and high-frequency spectrometers. Furthermore high-field and high-frequency cw EPR generally provides, by line shape analysis, shorter time windows down into the picosecond range for studying correlation times and fluctuating local fields over a wide temperature range. Such effects are associated with characteristic dynamic processes, e.g., protein and cofactor motion. Hence, structure–dynamics–function relations of biosystems can be elucidated in great detail, since transient intermediates can be observed in their working states at biologically relevant time scales. Pulsed high-field and high-frequency EPR as, for example, 2-D field-swept ESE spectroscopy, provides real-time access to specific cofactor and/or protein motions on the nanosecond time scale. Motional anisotropy can be resolved by measuring T_2, relaxation, which is governed by anisotropic interactions, such as hydrogen bonding along specific molecular axes within the binding site. High-field double-resonance techniques, such as ENDOR and PELDOR, add substantially to the capability of "classical" spectroscopic and diffraction techniques for determining the architecture of transient states of cofactors in their binding sites, i.e., their distance and relative orientation as well as function-related changes during the (photo)chemical reaction.

Acknowledgments

This paper is dedicated to George Feher in celebration of his 80th birthday (2004) and the 50th anniversary of his discovery of ENDOR (2006). Moreover, his fundamental contributions to an understanding of the primary processes in RCs from photosynthetic bacteria coined also our EPR and ENDOR work on photosynthesis. This is acknowledged with gratitude.

We thank Marco Flores, Jens Niklas and Maurice van Gastel (Mülheim an der Ruhr, Germany) as well as Jim Allen and Neal Woodbury (Tempe, AZ, USA) for providing RC preparations from site-specific mutants of *R. sphaeroides*. We gratefully acknowledge the support of the Deutsche Forschungsgemeinschaft in the frame of the priority programs SFB 498, SPP 1051 and the grant MO 132/13-2.

References

1. Feher G.: J. Chem. Soc. Perkin Trans. 2 **11**, 1861–1867 (1992)
2. Blankenship R.E.: Molecular Mechanisms of Photosynthesis. Oxford: Blackwell Science 2002.
3. Bixon M., Fajer J., Feher G., Freed J.H., Gamliel D., Hoff A.J., Levanon H., Möbius K., Nechushtai R., Norris J.R., Scherz A., Sessler J.L., Stehlik D.: Isr. J. Chem. **32**, 369–518 (1992)
4. Stowell M.H.B., McPhillips T.M., Rees D.C., Soltis S.M., Abresch E., Feher G.: Science **276**, 812–816 (1997)
5. Kirmeier C., Holten D.: Photosynth. Res. **13**, 225–260 (1987)
6. Kirmeier C., Bautista J.A., Laible P.D., Hanson D.K., Holten D.: J. Phys. Chem. B **109**, 24160–24172 (2005)
7. Paddock M.L., Isaacson R.A., Abresch E.C., Okamura M.Y.: Appl. Magn. Reson. **31**, 29 (2007)
8. Jortner J., Bixon M. (eds.): Electron Transfer: from Isolated Molecules to Biomolecules. Advances in Chemical Physics, vols. 106–107. New York: Wiley 1999.
9. Haffa A.L.M., Lin S., Williams J.C., Bowen B.P., Taguchi A.K.W., Allen J.P., Woodbury N.W.: J. Phys. Chem. B **108**, 4–7 (2004)
10. Lancaster C.R.D., Michel H. in: Handbook of Metalloproteins (Messerschmidt A., Huber R., Poulos T., Wieghardt K., eds.), p. 119. Chichester: John Wiley 2001.
11. Wakeham M., Jones M.: Biochem. Soc. Trans. **33**, 851–857 (2005)
12. Haffa A.L.M., Lin S., Williams J.C., Taguchi A.K.W., Allen J.P., Woodbury N.W.: J. Phys. Chem. B **107**, 12503–12510 (2003)
13. Paddock M.L., Chang C., Xu Q., Abresch E.C., Axelrod H.L., Feher G., Okamura M.Y.: Biochemistry **44**, 6920–6928 (2005)
14. Marcus R.A.: J. Chem. Phys. **24**, 966–978 (1956)
15. Michel-Beyerle M.-E. (ed.): The Reaction Center of Photosynthetic Bacteria: Structure and Dynamics. Berlin: Springer 1996.
16. Rautter J., Lendzian F., Schulz C., Fetsch A., Kuhn M., Lin X., Williams J.C., Allen J.P., Lubitz W.: Biochemistry **34**, 8130–8143 (1995)
17. Plato M., Möbius K., Michel-Beyerle M.-E., Bixon M., Jortner J.: J. Am. Chem. Soc. **110**, 7279–7285 (1988)
18. Levanon H., Möbius K.: Annu. Rev. Biophys. Biomol. Struct. **26**, 495–540 (1997)
19. Feher G.: Phys. Rev. **103**, 834–835 (1956)
20. Milov A.D., Ponomarev A.B., Tsvetkov Y.D.: Chem. Phys. Lett. **110**, 67–72 (1984)
21. Fuchs M.R., Schleicher E., Schnegg A., Kay C.W.M., Törring J., Bittl R., Bacher A., Richter G., Möbius K., Weber S.: J. Phys. Chem. B **106**, 8885–8890 (2002)
22. Schnegg A., Kay C.W.M., Schleicher E., Hitomi K., Todo T., Möbius K., Weber S.: Mol. Phys. **104**, 1627–1633 (2006)
23. Feher G., Okamura M.Y. in: The Photosynthetic Bacteria (Clayton R.K., Sistrom W.R., eds.), pp. 349–386. New York: Plenum Press 1978.
24. Schulz C., Müh F., Beyer A., Jordan R., Schlodder E., Lubitz W. in: Photosynthesis: Mechanisms and Effects (Garab G., ed.), pp. 767–770. Dordrecht: Kluwer 1998.
25. Paddock M.L., Rongey S.H., Feher G., Okamura M.Y.: Proc. Natl. Acad. Sci. USA **86**, 6602–6606 (1989)
26. Williams J.C., Haffa A.L.M., McCulley J.L., Woodburry N.W., Allen J.P.: Biochemistry **40**, 15403–15407 (2001)
27. Debus R.J., Feher G., Okamura M.Y.: Biochemistry **25**, 2276–2287 (1986)

28. Isaacson R.A., Abresch E.C., Lendzian F., Boullais C., Paddock M.L., Mioskowski C., Lubitz W., Feher G. in: The Reaction Center of Photosynthetic Bacteria (Michel-Beyerle M.-E., ed.), pp. 353–368. Berlin: Springer 1995.
29. Lubitz W., Feher G.: Appl. Magn. Reson. **17**, 1–48 (1999)
30. Lubitz W., Abresch E.C., Debus R.J., Isaacson R.A., Okamura M.Y., Feher G.: Biochim. Biophys. Acta **808**, 464–469 (1985)
31. Pople J.A., Beveridge D.L.: Approximate Molecular Orbital Theory. New York: McGraw Hill 1970.
32. Stewart J.J.P.: J. Comput.-Aided Mol. Des. **4**, 1–105 (1990)
33. Ridley J.E., Zerner M.C.: Theor. Chem. Acta **32**, 111–134 (1973)
34. Schreckenbach G., Ziegler T.: J. Phys. Chem. A **101**, 3388–3399 (1997)
35. Schreckenbach G., Ziegler T.: Theor. Chem. Acc. **99**, 71–82 (1998)
36. Patchkovskii S., Ziegler T.: J. Phys. Chem. A **105**, 5490–5497 (2001)
37. Malkina O.L., Vaara J., Schimmelpfennig B., Munzarová M.L., Malkin V.G., Kaupp M.: J. Am. Chem. Soc. **122**, 9206–9218 (2000)
38. Neese F., Munzarova M.L. in: The Quantum Chemical Calculation of NMR and EPR Properties (Kaupp M., Bühl M., Malkin V., eds.), p. 21. Weinheim: Wiley-VCH 2004.
39. Neese F.: J. Chem. Phys. **115**, 11080–11096 (2001)
40. van Lenthe E., Wormer P.E.S., van der Avoird A.: J. Chem. Phys. **107**, 2488–2498 (1997)
41. Neyman K.M., Ganyushin D.I., Matveev A.V., Nashzov V.A.: J. Phys. Chem. A **106**, 5022–5030 (2002)
42. te Velde G., Bickelhaupt F.M., Baerends E.T., Fonseca Guerra C.F., van Gisbergen S.J.A., Snijders J.G., Ziegler T.: J. Comput. Chem. **22**, 931–967 (2001)
43. Fuchs M.R., Schnegg A., Plato M., Schulz C., Müh F., Lubitz W., Möbius K.: Chem. Phys. **294**, 371–384 (2003)
44. Becke A.D.: Phys. Rev. A **38**, 3098–3100 (1988)
45. Lee C., Yang W., Parr R.G.: Phys. Rev. B **37**, 785–789 (1988)
46. Savitsky A., Kühn M., Duché D., Möbius K., Steinhoff H.J.: J. Phys. Chem. B **108**, 9541–9548 (2004)
47. Möbius K., Savitsky A., Fuchs M. in: Very High Frequency (VHF) ESR/EPR. Biological Magnetic Resonance, vol. 22 (Grinberg O., Berliner L.J., eds.), pp. 45–93. New York: Kluwer Academic/Plenum 2004.
48. Möbius K., Savitsky A., Schnegg A., Plato M., Fuhs M.: Phys. Chem. Chem. Phys. **7**, 19–42 (2005)
49. Prisner T.F., Rohrer M., Möbius K.: Appl. Magn. Reson. **7**, 167–183 (1994)
50. Burghaus O., Rohrer M., Götzinger T., Plato M., Möbius K.: Meas. Sci. Technol. **3**, 765–774 (1992)
51. Klette R., Törring J.T., Plato M., Möbius K., Bönigk B., Lubitz W.: J. Phys. Chem. **97**, 2015–2020 (1993)
52. Fuhs M., Schnegg A., Prisner T., Köhne I., Hanley J., Rutherford A.W., Möbius K.: Biochim. Biophys. Acta **1556**, 81–88 (2002)
53. Dubinskii A.A., Grishin Y.A., Savitsky A.N., Möbius K.: Appl. Magn. Reson. **22**, 369–386 (2002)
54. Fuchs M.R., Prisner T.F., Möbius K.: Rev. Sci. Instrum. **70**, 3681–3683 (1999)
55. Smith G.M., Riedi P.C. in: Electron Paramagnetic Resonance, vol. 17 (Gilbert B.C., Davies M.J., McLauchlan K.A., eds.), pp. 164–204. Specialist Periodical Reports. Cambridge: Royal Society of Chemistry 2000.
56. Disselhorst J.A.J.M., Vandermeer H., Poluektov O.G., Schmidt J.: J. Magn. Reson. A **115**, 183–188 (1995)
57. Rohrer M., Plato M., MacMillan F., Grishin Y., Lubitz W., Möbius K.: J. Magn. Reson. A **116**, 59–66 (1995)
58. Brunel L.-C., van Tol J., Angerhofer A., Hill S., Krzystek J., Maniero A.L. in: Very High Frequency (VHF) ESR/EPR. Biological Magnetic Resonance, vol. 22 (Grinberg O., Berliner L.J., eds.), pp. 465–505. New York: Kluwer Academic/Plenum 2004.
59. Lendzian F., Huber M., Isaacson R.A., Endeward B., Plato M., Bönigk B., Möbius K., Lubitz W., Feher G.: Biochim. Biophys. Acta **1183**, 139–160 (1993)
60. Burghaus O., Plato M., Rohrer M., Möbius K., MacMillan F., Lubitz W.: J. Phys. Chem. **97**, 7639–7647 (1993)

61. Hoff A.J., Deisenhofer J.: Phys. Rep. **287**, 1–247 (1997)
62. Huber M.: Photosynth. Res. **52**, 1–26 (1997)
63. Lubitz W., Lendzian F., Bittl R.: Acc. Chem. Res. **35**, 313–320 (2002)
64. Ivancich A., Artz K., Williams J.C., Allen J.P., Mattioli T.-A.: Biochemistry **37**, 11812–11820 (1998)
65. Huber M., Törring J.T.: Chem. Phys. **194**, 379–385 (1995)
66. Huber M., Törring J.T., Plato M., Finck U., Lubitz W., Feick R., Schenck C.C., Möbius K.: J. Sol. Energy Mater. Sol. Cells **38**, 119–126 (1995)
67. Artz K., Williams J.C., Allen J.P., Lendzian F., Rautter J., Lubitz W.: Proc. Natl. Acad. Sci. USA **94**, 13582–13587 (1997)
68. Müh F., Lendzian F., Roy M., Williams J.C., Allen J.P., Lubitz W.: J. Phys. Chem. B **106**, 3226–3236 (2002)
69. Möbius K., Biehl R. in: Multiple Electron Resonance Spectroscopy (Dorio M.M., Freed J.H., eds.), pp. 475–508. New York: Plenum 1979.
70. Gessner C., Lendzian F., Bönigk B., Plato M., Möbius K., Lubitz W.: Appl. Magn. Reson. **3**, 763–777 (1992)
71. Lin X., Murchinson H.A., Nagarajan V., Parson W.W., Allen J.P., Williams J.C.: Proc. Natl. Acad. Sci. USA **91**, 10265–10269 (1994)
72. Wang W., Belford R.L., Clarkson R.B., Davis P.H., Forrer J., Nilges M.J., Timken M.D., Walczak T., Thurnauer M.C., Norris J.R., Morris A.L., Zhang Y.: Appl. Magn. Reson. **6**, 195–215 (1994)
73. Huber M., Isaacson R.A., Abresh E.C., Gaul D., Schenck C.C., Feher G.: Biochim. Biophys. Acta **1273**, 108–128 (1996)
74. Chirino A.J., Lous E.J., Huber M., Allen J.P., Schenck C.C., Paddock M.L., Feher G., Rees D.C.: Biochemistry **33**, 4584–4593 (1994)
75. Fajer J., Borg D.C., Forman A., Dolphin D., Felton R.H.: J. Am. Chem. Soc. **95**, 2739–2741 (1973)
76. McDowell L.M., Gaul D., Kirmaier C., Holten D., Schenck C.C.: Biochemistry **30**, 8315–8322 (1991)
77. Bratt P.J., Ringus E., Hassan A., van Tol H., Maniero A.-L., Brunel L.-C., Rohrer M., Bubenzer-Hange C., Scheer H., Angerhofer A.: J. Phys. Chem. B **103**, 10973–10982 (1999)
78. Gulin V.I., Dikanov S.A., Tsvetkov Y.D., Evelo R.G., Hoff A.J.: Pure Appl. Chem. **64**, 903–906 (1992)
79. Plato M., Möbius K.: Chem. Phys. **197**, 289–295 (1995)
80. Müh F., Bibikova M., Lendzian F., Oesterhelt D., Lubitz W. in: Photosynthesis: Mechanisms and Effects (Garab G., ed.), pp. 763–766. Dordrecht: Kluwer 1998.
81. Müh F., Bibikova M., Schlodder E., Oesterhelt D., Lubitz W.: Biochim. Biophys. Acta **1459**, 191–201 (2000)
82. Atherton N.M.: Principles of Electron Spin Resonance. New York: Ellis Horwood 1993.
83. Isaacson R., Lendzian F., Abresch E., Lubitz W., Feher G.: Biophys. J. **69**, 311–322 (1995)
84. Rohrer M., Gast P., Möbius K., Prisner T.F.: Chem. Phys. Lett. **259**, 523–530 (1996)
85. Rohrer M., MacMillan F., Prisner T.F., Gardiner A.T., Möbius K., Lubitz W.: J. Phys. Chem. B **102**, 4648–4657 (1998)
86. Burghaus O., Toth-Kischkat A., Klette R., Möbius K.: J. Magn. Reson. **80**, 383–388 (1988)
87. Prisner T.F., van der Est A., Bittl R., Lubitz W., Stehlik D., Möbius K.: Chem. Phys. **194**, 361–370 (1995)
88. Stehlik D., Möbius K.: Annu. Rev. Phys. Chem. **48**, 745–784 (1997)
89. Weber S. in: Electron Paramagnetic Resonance, vol. 17 (Gilbert B.C., Davies M.J., McLauchlan K.A., eds.), pp. 43–77. Specialist Periodical Reports. Cambridge: Royal Society of Chemistry 2000.
90. Lubitz W. in: Electron Paramagnetic Resonance, vol. 19 (Gilbert B.C., Davies M.J., Murphy D.M., eds.), pp. 174–242. Specialist Periodical Reports. Cambridge: Royal Society of Chemistry 2004.
91. van der Est A.: Biochim. Biophys. Acta **1507**, 212–225 (2001)
92. Thurnauer M.C., Poluektov O.G., Kothe G. in: Very High Frequency (VHF) ESR/EPR. Biological Magnetic Resonance, vol. 22 (Grinberg O., Berliner L.J., eds.), pp. 166–206. New York: Kluwer Academic/Plenum 2004.
93. Denysenkov V.P., Prisner T.F., Stubbe J., Bennati M.: Appl. Magn. Reson. **29**, 375–384 (2005)

94. Denysenkov V.P., Prisner T.F., Stubbe J., Bennati M.: Proc. Natl. Acad. Sci. USA **103**, 13386–13390 (2006)
95. Kamlowski A., Zech S.G., Fromme P., Bittl R., Lubitz W., Witt H.T., Stehlik D.: J. Phys. Chem. B **102**, 8266–8277 (1998)
96. Stehlik D., Bock C.H., Petersen J.: J. Phys. Chem. **93**, 1612–1619 (1989)
97. Hore P.J., Hunter D.A., McKie C.D., Hoff A.J.: Chem. Phys. Lett. **137**, 495–500 (1987)
98. Closs G.L., Forbes M.D.E., Norris J.R.: J. Phys. Chem. **91**, 3592–3599 (1987)
99. Kandrashkin Y., van der Est A.: Spectrochim. Acta A **57**, 1697–1709 (2001)
100. Bittl R., Zech S.G.: J. Phys. Chem. B **101**, 1429–1436 (1997)
101. Schweiger A., Jeschke G.: Principles of Pulse Electron Paramagnetic Resonance. Oxford: University Press 2001.
102. Schnegg A., Fuhs M., Rohrer M., Lubitz W., Prisner T.F., Möbius K.: J. Phys. Chem. B **106**, 9454–9462 (2002)
103. Stoll S., Schweiger A.: J. Magn. Reson. 178, 42–55 (2006)

Authors' address: Klaus Möbius, Fachbereich Physik, Freie Universität Berlin, Arnimallee 14, 14195 Berlin, Germany
E-mail: moebius@physik.fu-berlin.de